RSC Applied Polymers

ROYAL SOCIETY OF CHEMISTRY

REVIEW

View Article Online
View Journal | View Issue

Check for updates

Cite this: *RSC Appl. Polym.*, 2025, **3**, 549

Recent material development and applications of conjugated polyelectrolytes by leveraging electronic and ionic transport properties

Chibin Zhang,[a] Liang Yao,[a] Mingrui Pu*[a,b] and Cheng Zhou *[a]

Received 20th January 2025,
Accepted 13th March 2025

DOI: 10.1039/d5lp00012b

rsc.li/rscapplpolym

Conjugated polyelectrolytes (CPEs) are a distinct class of organic materials featuring a π-conjugated backbone and ionic functional groups, enabling simultaneous electronic and ionic transport. This dual conductivity, governed by molecular design, makes CPEs highly versatile for a wide range of applications. The interplay between backbone conjugation and side-chain polarity allows fine-tuning of charge transport, significantly influencing their performance in electronic and energy storage devices. This review highlights recent advances in CPE material design, focusing on backbone evolution and side-chain engineering. We further explore key applications of CPEs, including organic photovoltaics, organic electrochemical transistors, and lithium-ion batteries, emphasizing the structural requirements for each field. Their current challenges and future opportunities are discussed, underscoring the critical role played by CPEs in next-generation optoelectronic and energy technologies.

Open Access Article. Published on 14 März 2025. Downloaded on 28.01.2026 01:53:57.
This article is licensed under a Creative Commons Attribution-NonCommercial 3.0 Unported Licence.

1. Introduction

Conjugated polyelectrolytes (CPEs) have garnered significant attention in recent years due to their exceptional charge and ion transport properties, positioning them as promising materials for a diverse array of emerging applications, including photovoltaics,[1–4] energy storage,[5–7] and bioelectronics.[8–10] CPEs are a class of organic macromolecular materials characterized by a conjugated backbone and polar side chains, which confer excellent electrical properties and processability.[11] Typically, the polymer backbone adopts a completely planar configuration, allowing the π-electron orbitals of adjacent atoms to overlap effectively, thereby forming a delocalized π-channel that facilitates a conductive pathway for charge carriers. The development of conductive polymers can be traced back to the pioneering work of Japanese scientist Hideki Shirakawa, with significant contributions from American scientists Alan Heeger and Alan MacDiarmid. Their groundbreaking research in conductive polymers was recognized with the Nobel Prize in chemistry in 2000, underscoring their profound impact on materials science and the scientific community.[12,13]

Building upon this foundation, Heeger categorized conductive polymers into three generations. The first generation was exemplified by polyacetylene, which laid the groundwork for conductive polymer research. The second generation introduced soluble and processable polymers and copolymers, enhancing their applicability in various processing techniques (Fig. 1). The third generation comprises semiconductors with more complex structures, further advancing the functionality and performance of conductive polymers (Fig. 2).[14] The chemical structure of the CPE backbone plays a pivotal role in determining the conformations of the polymer chain, which in turn significantly influences key optoelectronic properties. These properties are critical as they directly affect molecular packing and energy levels, which are essential for device performance.[15,16] Through strategic side-chain engineering, CPEs exhibit enhanced solubility, and the incorporation of polar side chains facilitates processing in orthogonal solvents.[1,17] Consequently, CPEs not only retain the inherent advantages of organic semiconductors, such as excellent processability and tunable energy levels, but also possess the unique dual capability to efficiently conduct both ions and electrons.[18] This dual functionality renders them highly promising for a wide range of emerging applications.[19] The presence of polar groups not only aids in processing but also expands their applicability in organic multilayer devices, including organic solar cells (OSCs) and perovskite solar cells (PSCs).[20–23] However, when employed as interfacial materials, the focus is often predominantly on their electronic transport properties, with their ionic transport characteristics frequently being overlooked.[19] In the context of CPEs, conductivity is highly

[a]*Institute of Polymer Optoelectronic Materials & Devices, Guangdong Basic Research Center of Excellence for Energy & Information Polymer Materials, State Key Laboratory of Luminescent Materials & Devices, South China University of Technology, Guangzhou 510640, P. R. China. E-mail: czhou@scut.edu.cn*
[b]*Guangzhou China Ray Optoelectronic Materials Co., Ltd, Guangzhou 510670, P. R. China. E-mail: pumingrui1@tcl.com*

© 2025 The Author(s). Published by the Royal Society of Chemistry

Open Access Article. Published on 14 März 2025. Downloaded on 28.01.2026 01:53:57.
This article is licensed under a Creative Commons Attribution-NonCommercial 3.0 Unported Licence.

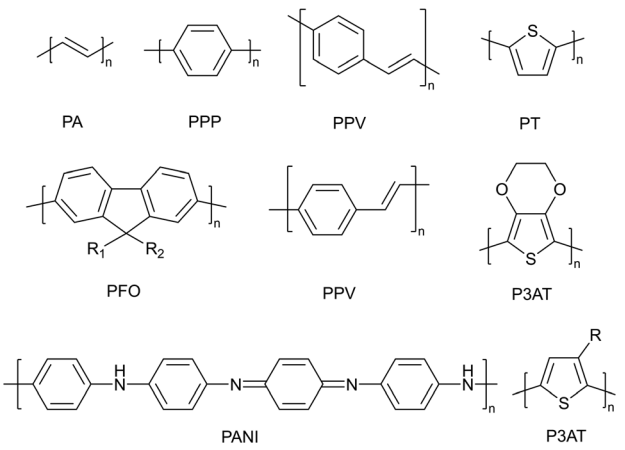

Fig. 1 Structures representing second-generation organic semiconductors.

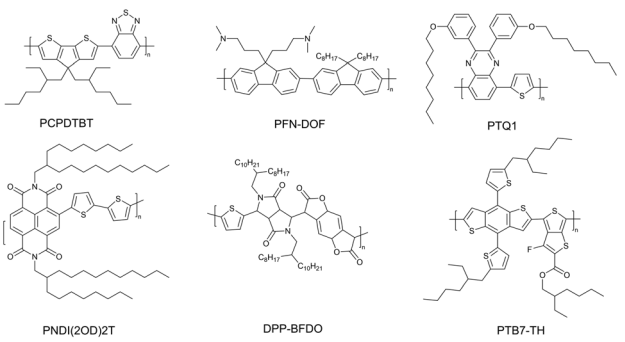

Fig. 2 Structures representing third-generation organic semiconductors.

dependent on the doping state. For instance, in applications such as organic electrochemical transistors (OECTs), ions are injected from the electrolyte into the organic film, altering the doping state and, consequently, its conductivity. Therefore, the ability to effectively couple ionic and electronic transport is essential.[24,25] In battery electrodes, CPEs must not only exhibit high electronic conductivity but also demonstrate significant ionic conductivity to optimize device performance.[5,26,27] Additionally, due to their excellent biocompatibility, tunable energy levels, and favorable optoelectronic properties, CPEs have demonstrated significant potential in applications such as electron transfer, light energy conversion, biofuel cells, and bioelectronic catalysis.[11,28,29]

Advancements in this field hinge on a deeper understanding of the interrelations between ionic transport, electronic transport, and ionic–electronic coupling, as well as the influence of processing methods, synthetic design, and microstructure on these phenomena.[30–33] Current knowledge encompasses well-established concepts, such as the dependence of electronic transport on ionic–electronic coupling, as well as emerging areas like the role played by synthetic design in ionic transport. However, there remain largely unexplored regions, such as the impact of processing techniques on ionic transport.[19]

In this review, we provide a comprehensive overview of the development and characterization of CPEs, with a particular emphasis on their ionic and electronic transport properties. We examine the fundamental mechanisms of ion–electron coupling that underpin charge transport, addressing both electronic and ionic contributions. Additionally, we explore the structure–property relationships that govern the behavior of CPEs and their implications for various applications. Looking ahead, we highlight the necessity for further research into these structure–performance correlations, which are critical for guiding the future development and application of CPEs in advanced ionic and electronic devices.

2. Materials

Untreated conductive polymers exhibit insulating properties due to their large energy gaps. Oxidative (p-type) or reductive (n-type) doping introduces new energy levels, such as polarons, significantly enhancing conductivity to semiconductor or metallic levels (10–10 000 S cm^{-1}). The first-generation polyacetylene, limited by processing challenges, was succeeded by second-generation polymers featuring thiophene/phenyl derivative-based main chains and side chains to improve solubility. Cao *et al.* further advanced processability through anion-induced doping (*e.g.*, dodecylbenzenesulfonic acid, DBSA), enabling tunable conductivity (10^{-1}–100 S cm^{-1}) while achieving a balance between high conductivity and processability in multi-blend systems. The third generation of organic semiconductors is characterized by more intricate molecular architectures, with a higher number of atoms in the repeating units. Through systematic studies of the charge transport and photophysical properties of second-generation conjugated polymers, the foundation for organic electronics was established. Subsequently, conjugated polymers with more complex repeating units were developed, forming the third generation of semiconductor polymers. A particularly notable class within this category is CPE, which can simultaneously transport both ions and electrons. Traditional CPEs are often heterogeneous blends or complexes comprising an electrically conducting π-conjugated polymer and an ionically conductive polyelectrolyte, representing the most widely studied class of conjugated polymers.[19] By integrating conventional conjugated polymer design approaches, single-component ion–electron conductor polyelectrolytes have been developed by attaching polar groups to the conjugated backbone of traditional polymers *via* alkyl or ether chains.[18] Structural modifications to the chemical backbone or side chains allow CPEs to exhibit a wide range of mobilities, capacitances, and oxidation/reduction onset values. Additionally, the coupling of electronic and ionic charge carriers creates an intrinsic transduction mechanism, where ionic signals directly influence conductivity (Fig. 3).[31] Thus, balancing the interactions between the main chain and side chains is crucial for the effective design of CPEs. The following section will discuss the design principles governing these materials.

© 2025 The Author(s). Published by the Royal Society of Chemistry

Open Access Article. Published on 14 März 2025. Downloaded on 28.01.2026 01:53:57.
This article is licensed under a Creative Commons Attribution-NonCommercial 3.0 Unported Licence.

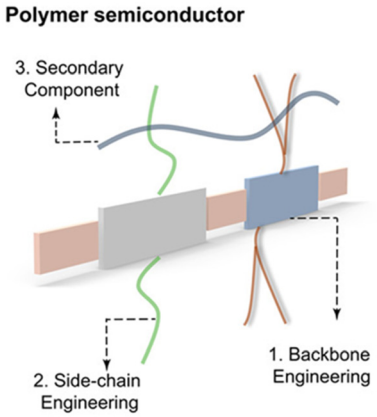

Fig. 3 Polymer semiconductors consist of conjugated backbones and nonconjugated side chains. Reprinted (adapted) with permission from ref. 34. Copyright 2022 American Chemical Society.

2.1 Backbone engineering

The energy level distribution and electronic conductivity of CPEs are largely determined by the conjugated backbone. In organic semiconductors, charge carriers are transported along the conjugated polymer backbone *via* intra-chain transport and inter-chain π–π stacking interactions (inter-chain charge transport).[35] The chemical structure of independent organic semiconductor molecules is typically characterized by alternating single and double bonds, where the σ bonds form the molecular backbone, and the conjugated π electrons are delocalized, creating conductive pathways for mobile charges within the polymer.[36] Like atoms, molecules possess discrete energy levels known as molecular orbitals. Among these, the highest occupied molecular orbital (HOMO) and the lowest unoccupied molecular orbital (LUMO) are particularly significant, as the relevant electron and exciton processes in organic devices typically involve transitions between these levels.[8,37]

For most CPEs, the conjugated backbone consists predominantly of p-type transport units, often made up of donor entities such as thiophene, carbazole, or triphenylamine.[20,38–41] In contrast, n-type transport materials typically include acceptor units such as perylenediimide (PDI), fluorene, and 3,7-dihydrobenzo[1,2-*b*:4,5-*b*′]difuran-2,6-dione (H-BFDO).[3,22,42] The optoelectronic properties of CPEs, including absorption, emission spectra, and charge transport capabilities, can be manipulated by customizing their π-conjugated backbone structures.[17] Connecting electron-donating and electron-accepting groups to the backbone is the most direct method for tuning the HOMO and LUMO energy levels of semiconductor polymers.[43–46] As shown in Fig. 4, Liu *et al.* synthesized a series of benzodithiophene–thienothiophene copolymers with varying degrees of fluorine decoration. They observed that incorporating fluorine into the thienothiophene units deepened the HOMO energy levels without significantly affecting the bandgap or light-harvesting properties of the polymers.[47] Huang *et al.* designed and synthesized a fused nonacyclic non-

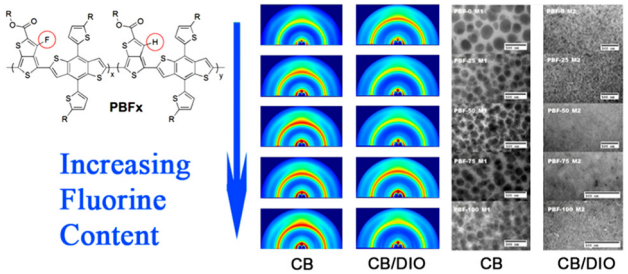

Fig. 4 Molecular structure, GIXD scattering images of PBFx polymers and blends and TEM images of PBFx:PCBM blends. Reprinted (adapted) with permission from ref. 46. Copyright 2014 American Chemical Society.

fullerene acceptor, TfIF-4Cl, *via* end-group chlorination. Compared with its fluorinated counterpart (TfIF-4F), the introduction of chlorine not only led to deeper energy levels and red-shifted absorption but also improved the morphological properties and molecular packing ability.[48] Alternating donor (D) and acceptor (A) units along the polymer backbone in a regular pattern is a highly effective strategy for designing low-bandgap semiconducting polymers.[49–51] The interactions between the D and A components facilitate π electron delocalization, leading to a quinoid mesomeric structure along the polymer main chain, resulting in a reduced bandgap (Fig. 5).[43,52] Jiang *et al.* synthesized a D–A–D type near-infrared (NIR) luminescent molecule, where the near-planar arrangement of the donor and acceptor units enhanced orbital overlap and increased radiative transition rates and fluorescence efficiency.[53]

As discussed earlier, intramolecular charge transfer along the polymer backbones is directly correlated with the energy levels of semiconducting polymers and can be enhanced by incorporating donor–acceptor (D–A) structures. Additionally, intermolecular charge transfer, which occurs *via* a hopping mechanism facilitated by the overlap of π electrons between adjacent backbones, is crucial for charge mobility.[43] High conductivity is achieved through strong intrachain electron transport and moderate interchain conductivity, which depends on the face-to-face alignment of the polymer chains. In contrast, conductivity between widely spaced chains is typically low and

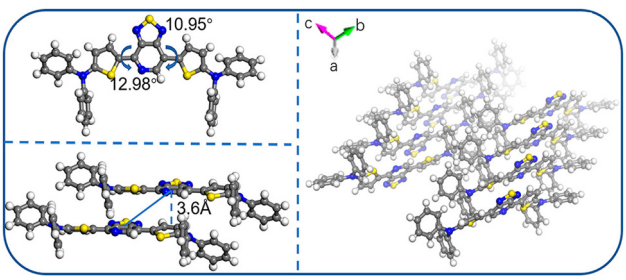

Fig. 5 Single-crystal structure of the compound DTPS-PT. Reprinted (adapted) with permission from ref. 52. Copyright 2019 American Chemical Society.

Open Access Article. Published on 14 März 2025. Downloaded on 28.01.2026 01:53:57.
This article is licensed under a Creative Commons Attribution-NonCommercial 3.0 Unported Licence.

often overlooked.[1] By carefully designing the main chain, it is possible to regulate both the energy levels and mobility of the polymer.[54,55]

Generally, strategies to enhance the electronic conductivity of semiconductor polymers rely on increasing the carrier mobility of holes or electrons in p-type and n-type materials, respectively. Features such as greater planarity, longer conjugation lengths, narrower bandgaps, and higher inter-chain order typically result in increased charge carrier mobility, thereby improving conductivity.[38,56–58] Although the contributions of inter-chain and intra-chain transport to polymer device performance remain uncertain, high crystallinity and optimized face-to-face alignment are critical factors for achieving good conductivity.[59] As shown in Fig. 6, Iain *et al.* engineered a semiconducting polythiophene that assembled into large crystalline domains during crystallization from a liquid-crystal phase. This material featured an extended, planar π-electron system, facilitating close intermolecular π–π stacking and high charge carrier mobility.[60] Using a heterocycle with a nitrogen atom as the acceptor unit, Jiang *et al.* reported an electron-deficient [1,2,5]thiadiazolo[3,4-*c*]pyridine (PT) oriented variably relative to the donor triphenylamine (TPA), leading to distinct asymmetric regio-isomers. Changes in the connection points between donor and acceptor units resulted in twisted structures that significantly affected photophysical properties.[57]

2.2 Side chain engineering

Side chains were initially designed to improve the solubility of conjugated polymers. Compared with linear alkyl chains, branched alkyl chains—such as 2-ethylhexyl, 2-hexyldecyl, 2-octyldodecyl, and 2-decyltetradecyl—have been shown to significantly enhance the solubility of these polymers.[61–63] However, researchers soon recognized that side chains also play a crucial role in influencing the conformational properties of the polymer chains, as well as their behavior in solution-state aggregation and solid-state molecular packing.[2,38,64–67] For example, Jin *et al.* introduced a novel approach for side-chain engineering in DPP-based D–A type conjugated polymers. By replacing the bulky branched alkyl chains with linear chains at each DPP unit, they synthesized PDPPSe-10 and PDPPSe-12. Their findings showed that: (i) the substitution of bulky branching chains with linear ones reduced steric hindrance, leading to more planar and rigid conjugated backbones; (ii) the use of linear alkyl chains facilitated side-chain interdigitation; and (iii) the interchain packing order and thin film crystallinity of PDPPSe-10 and PDPPSe-12 were significantly improved compared with the original PDPPSe polymer. These structural modifications contributed to a remarkable enhancement in charge mobilities for PDPPSe-10 and PDPPSe-12. Similarly, Jin *et al.* designed two narrow-bandgap conjugated polymers based on NT, incorporating a donor–acceptor (D–A) architecture with electron-accepting units. These copolymers, NT812 and NT1014, featured different side chains (2-octyldodecane and 2-decyltetradecane, respectively) on the thiophene units. Notably, NT812 exhibited significantly higher efficiency than NT1014, attributed to the "face-to-face" alignment of the NT812 polymer chains, which enhanced device performance (Fig. 7).[68] Additionally, Pang *et al.* investigated a series of donor polymers based on difluorobenzotriazole, where slight variations in side-chain atom substitutions led to marked differences in aggregation behavior, blend heterojunction morphology, and device performance (Fig. 8).[69]

In contrast to alkyl chains, polar side chains tend to confer better solubility in water and alcohols. Surfactant-like side groups, for example, enhance solubility in highly polar solvents and substantially influence the physical and chemical properties of conjugated polymers. Furthermore, they facilitate processing with environmentally friendly solvents.[23,70] The incorporation of polar groups also imparts strong interfacial modification capabilities to CPEs.[17] In certain cases, polar groups lead to self-doping polymers, preventing phase separ-

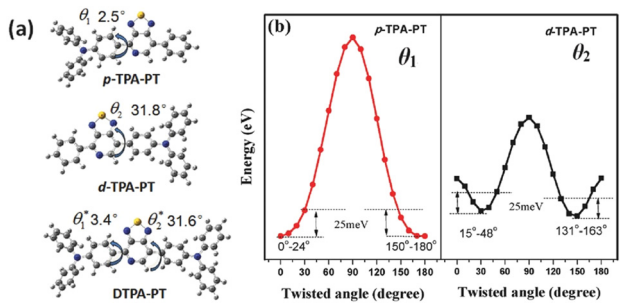

Fig. 6 (a) DFT-optimized geometries and D–A twist angles of p-TPA-PT, d-TPA-PT, and DTPA-PT. (b) The ground-state energies of p-TPA-PT, d-TPA-PT at different D–A torsion angles in the gas phase, using the cam-b3lyp method and a full geometrical optimization at each twist angle.[60]

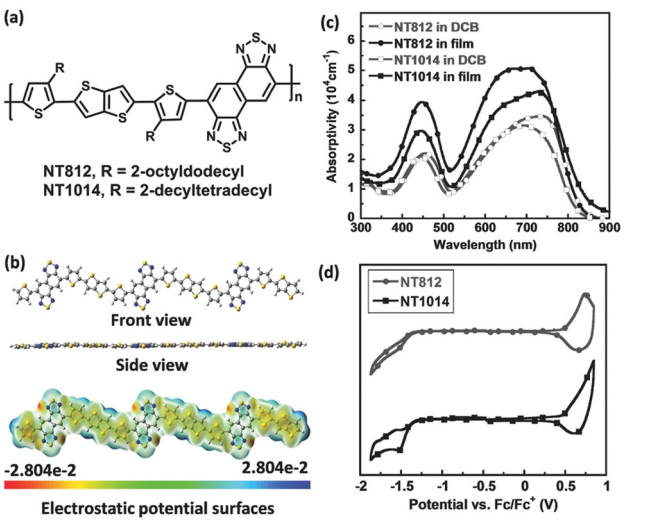

Fig. 7 (a) Molecular structures of copolymers NT812 and NT1014. (b) Calculated molecular geometry and electronic potential surface of BTTT-NT trimer. (c and d) Grazing incidence X-ray diffraction patterns of NT812:$PC_{71}BM$ (c) and NT1014:$PC_{71}BM$ (d).[38]

© 2025 The Author(s). Published by the Royal Society of Chemistry

Open Access Article. Published on 14 März 2025. Downloaded on 28.01.2026 01:53:57.
This article is licensed under a Creative Commons Attribution-NonCommercial 3.0 Unported Licence.

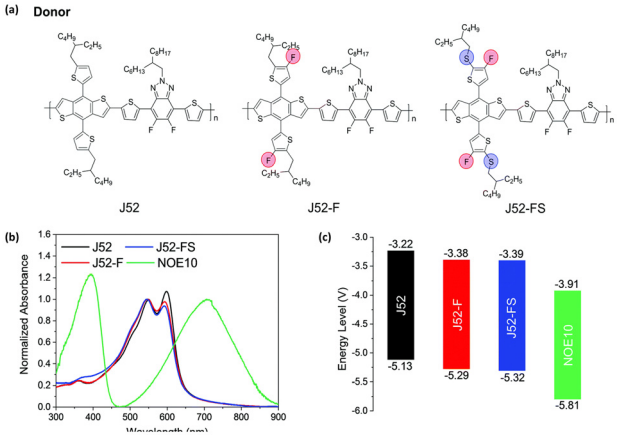

Fig. 8 (a) Molecular structures of copolymers. (b) Optical absorption spectra of thin films; (c) energy level diagram of J52, J52-F, J52-FS, and NOE10.[69]

ation and further enhancing conductivity.[22] For instance, P3HT, a widely used hole-transport material in perovskite and organic photovoltaic devices, typically requires doping to overcome its inherently low conductivity.[71,72] However, its hydrophobic nature and poor electrical conductivity in thin films lead to charge recombination and poor device performance.[73–75] To address these challenges, Hidenori Okuzaki's group at Yamanashi University developed a self-doped conductive polymer, S-PEDOT, containing alkyl sulfate side chains. S-PEDOT exhibits exceptional solubility in water and achieves a high conductivity of 1089 S cm^{-1} without the need for additional dopants. Moreover, the ionic components of the side chains, including their counterions, significantly impact the physical and chemical properties of CPEs.[76] For example, Yang *et al.* exchanged the bromide ions in water-soluble conjugated polymer (WSCP) with $CF_3SO_3^-$, $BArF_4^-$, and BIm_4^-, leading to an increase in counterion size, which reduced interchain contact, suppressed aggregation, and enhanced the photoluminescent quantum yield of the films. Conductive atomic force microscopy measurements further revealed that hole mobility and charge injection barrier height in the films were dependent on the counterion used.[77]

The properties of counterions can also influence the doping ability of CPEs, thereby affecting charge transport characteristics. Liang *et al.* introduced oxoammonium salts ($TEMPOX^+$–, where X = Br and TFSI) as secondary dopants to systematically modulate conductivity, work function, morphology, and the performance of PEDOT:PSS-based organic electrochemical transistors (OECTs). The presence of oxoammonium salts improved transfer characteristics in OECTs, with their concentration-dependent effects on device performance.[78]

Traditional CPEs typically enhance hydrophilicity by incorporating ionic chains or polyethylene glycol chains. However, this strategy often introduces insulating alkyl chains, resulting in microphase separation between the side chains and the main chain at the nanoscale. To address this issue, early work by Timothy *et al.* developed a series of novel water-soluble n-type conjugated polymers featuring pyridine-phenyl units. These polymers facilitated charge carrier formation in the main chain through the introduction of pyridine salts, significantly improving solubility without requiring doping (Fig. 9). These materials displayed high electron affinities, reversible redox behavior, high conductivities, and efficient electron mobilities.[79–81] Building on this work, Lei *et al.* developed an n-type water-soluble semiconductor polymer, P(PyV), which featured a cationic main chain with chloride ion counterions and no side chains. The P(PyV)-H polymer demonstrated outstanding n-type OECT performance, with μC^* values up to 120 F cm^{-1} V^{-1} s^{-1}, on/off ratios exceeding 10^7, and response times (τ_{on}/τ_{off}) of 1.58/0.18 ms, setting a new benchmark for n-type semiconducting polymers.[82]

Future designs of CPEs should carefully balance the relationship between side chains and the main chain, as both the structure and properties of the CPE backbone, in conjunction with the chemical characteristics of the side chains, collectively determine the material's physical, chemical, and optoelectronic performance.[52]

2.3 Material categories

In the following sections, we will explore the relationship between structure and performance by classifying CPEs according to their backbone structure.

2.3.1 Polythiophene. Polythiophene and its derivatives have garnered significant attention in device applications due to their high stability in undoped states, ease of structural modification, and solution processability. Notably, poly(3-hexylthiophene) (P3HT) has become one of the most cost-effective materials, attributed to its simple chemical structure and straightforward synthesis.[83–87] This enables large-scale fabrication through various eco-friendly polymerization methods. As a result, P3HT has emerged as the only polymer to date that can be synthesized at scales exceeding 1 kg, making it a central material in organic photovoltaic (OPV) research and organic thin-film transistors.[59,88,89] However, P3HT faces significant challenges in the development of all-polymer solar cells (all-PSCs), primarily due to its narrow absorption range in the visible spectrum and its inherently high-lying highest occupied molecular orbital (HOMO) level (approximately 5 eV). These limitations complicate the process of matching appro-

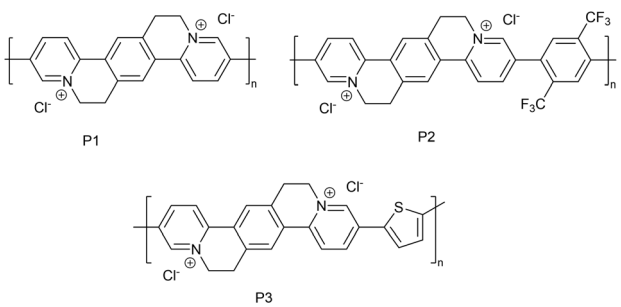

Fig. 9 Structures of polymer P1 and copolymer P2 and P3.

Open Access Article. Published on 14 März 2025. Downloaded on 28.01.2026 01:53:57.
This article is licensed under a Creative Commons Attribution-NonCommercial 3.0 Unported Licence.

priate polymer acceptors and controlling morphology, leading to consistently low device performance. Despite these obstacles, the low cost and scalability of P3HT remain promising factors for advancing the industrial-scale production of organic solar cells.

PEDOT:PSS is another well-established conducting polymer that is renowned for its exceptional electronic and optical properties. PEDOT was first introduced by Bayer AG scientists in a patent in 1988.[90] It was developed as an alternative to polythiophene in order to mitigate α–β and β–β coupling during the oxidative polymerization of thiophene. By substituting positions 3 and 4 of the thiophene ring, PEDOT demonstrates improved resistance to degradation by oxygen and water.[91,92] In a similar fashion to the concept of anion-induced processing, poly(styrene sulfonate) (PSS) serves as a matrix for PEDOT, facilitating its formation into an aqueous dispersion (Fig. 10). PEDOT:PSS is typically synthesized through a two-step process: the preparation of PSS followed by the oxidative polymerization of PEDOT. This not only forms a strong electrostatic association between PEDOT and PSS, but also uses PSS as a counterion to stabilize the doped PEDOT.[91] The combined characteristics of PEDOT, such as its adjustable work function and high thermoelectric performance, make it a versatile material with wide applications in organic electronics.[93] Its unique chemical structure also provides outstanding environmental stability, which has led to its widespread use in various optoelectronic devices.[94] In organic solar cells, PEDOT is commonly employed as an electrode modification layer to enhance charge transport efficiency.[95–98] In organic light-emitting diodes (OLEDs), PEDOT is used as a hole injection layer, significantly improving both luminous efficiency and operational lifetime.[99–102] Additionally, the excellent processability and tunable doping characteristics of PEDOT position it as a promising material in emerging fields such as flexible electronics[91,103] and bioelectronics,[91,104] solidifying its role as a foundational material driving advancements in organic optoelectronics.[105] However, the encapsulation of PSS typically leads to a reduction in the conductivity of PEDOT. This necessitates enhancement techniques, such as solvent treatment, acid treatment, and secondary doping, to improve its conductivity.[106–108] Moreover, phase separation between the ion-conducting PSS and the electron-conducting PEDOT results in the formation of two distinct phases. This separation reduces the ionic–electronic coupling (capacitance) between the two components, thereby limiting its suitability for new applications, particularly in bioelectronics.[109]

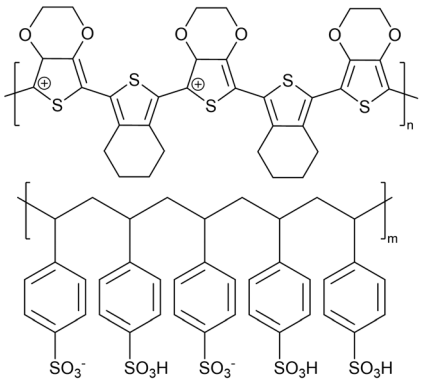

Fig. 10 (a) Chemical structures of PEDOT and PSS.

2.3.2 Phenyl derivatives. Phenyl derivatives are a class of organic compounds that contain a phenyl group ($-C_6H_5$) attached to various functional groups or molecular structures. In the field of organic semiconductors, phenyl derivatives play a crucial role due to their conjugated π-electron systems, which contribute to efficient charge transport properties. The introduction of phenyl groups or their derivatives can enhance molecular planarity, promote π–π stacking interactions, and improve charge mobility within semiconductor materials.

One of the most widely studied phenyl derivatives is poly (phenylenevinylene) (PPV), which is used in various fields, including optoelectronic devices. PPV is typically synthesized *via* two routes: the Wessling method and the Gilch method. The Wessling route involves the treatment of dimethylsulfonium salts with an equimolar amount of a base to form a soluble precursor polymer, which is then thermally processed to obtain conjugated PPV. The Gilch method, on the other hand, involves the treatment of α,α-dihalo-*p*-xylene with potassium *tert*-butoxide in an organic solvent. Alkyl or alkoxy substituents are commonly introduced onto the aromatic ring to improve the solubility of PPV.[110] One of the most extensively studied PPV derivatives is poly(1-methoxy-4-(2-ethylhexoxy)-*p*-phenylene vinylene) (MEH-PPV), which features asymmetric side chains that confer high solubility in common organic solvents.[111]

Introducing amino groups to phenyl rings significantly enhances hole mobility due to the strong electron-donating ability of the nitrogen atoms in the structure. Compared with other conjugated polymers, polyaniline is readily available, easy to synthesize, and exhibits good environmental stability, making it amenable for doping for controlled conductivity. Over the past three decades, extensive research has been conducted on the modification and application of polyaniline, leading to its widespread use in fields such as light-emitting diodes,[112] supercapacitors,[113] and organic solar cells.[114] In 1987, MacDiarmid and colleagues proposed a model for the structure of polyaniline that featured the coexistence of benzenoid (reduced unit) and quinoid (oxidized unit) structural units. Polyaniline undergoes redox reactions in which ions from dopants penetrate the polymer, neutralizing the electrons on the main chain. This allows polyaniline to reversibly transition from an insulating state to a conductive state.[115] However, the solubility of polyaniline remains limited. To address this issue, Cao *et al.* introduced the concept of anion-induced processing, utilizing dodecylbenzenesulfonic acid as a dopant to create stable and processable multi-blends. These multi-blends exhibit a unique combination of properties, enabling conductivity to be conventionally controlled over a broad range (from 10^{-1} to 100 S cm^{-1}), thus overcoming the challenge of balancing high conductivity and processability in conductive polymers.[116]

© 2025 The Author(s). Published by the Royal Society of Chemistry

Open Access Article. Published on 14 März 2025. Downloaded on 28.01.2026 01:53:57.
This article is licensed under a Creative Commons Attribution-NonCommercial 3.0 Unported Licence.

2.3.3 Polyfluorenes. CPEs based on the fluorenyl structural unit have garnered significant research attention and are widely used in cathode interfacial layers.[17] As previously mentioned, WSCPs, such as PFN-Br, consist of two key structural components: a π-conjugated main chain and surfactant-like side groups, including amino, dihydroxyethylamino, phosphate, carboxyl, quaternary ammonium, anionic carboxyl, sulfonic, and zwitterionic groups. The π-conjugated main chain governs the inherent optoelectronic properties of WSCPs, such as absorption and emission spectra, energy band structure, and charge transport characteristics, while the surfactant-like side groups provide unique solubility in highly polar solvents.[17] In 2004, Cao *et al.* designed and synthesized a series of novel water-soluble/alcohol-soluble conjugated polymers—P1 (PFN), P2 (PFN-Br), P3, and P4 (PFQ-Br)—which were employed as electron transport layers in organic light-emitting diodes, yielding excellent performance.[117] The quaternary ammonium salt side chains not only enhance the dispersion and solubility of the CPEs but also promote interactions between the polar side chains in the CPEs and the metal electrodes. This interaction improves charge transport/transfer from the conjugated polymer to the metal electrodes, thereby enhancing work function modification capabilities.[85] Furthermore, these side chains influence main chain stacking and doping, significantly improving conductivity. Xue *et al.* studied the formation of the β-phase in poly(diarylfluorene) with varying side chain lengths. The balance between steric hindrance from octyl side chains and supramolecular interactions between chains is linked to the extended conjugation length and better control over the conformation and aggregation of organic conjugated polymer chains, which facilitates exciton migration between β-phase polyfluorene units.[118] Tang *et al.* designed n-type self-doped CPEs by copolymerizing the open-shell diradical unit benzobisthiadiazo (BBT) with fluorenes. As shown in ESR spectra, the BBT diradical unit strengthens the interaction between the polar side chains and the conjugated backbone, promoting the self-doping process of conjugated polyelectrolytes (Fig. 11).[119]

2.3.4 Naphthalene diimide (NDI) and perylene diimide (PDI). The development of n-type organic semiconductors has historically lagged behind p-type semiconductors. Aromatic diimides, such as NDI and PDI, represent some of the most important classes of n-type organic materials. NDI- and PDI-based derivatives have emerged as promising materials for electron transport layers due to their well-aligned energy levels and excellent electron transport properties.[120,121] After years of structural optimization, the highest electron mobility of small molecules based on NDI and PDI has reached 8.69 $cm^2\ V^{-1}\ s^{-1}$ and 10.8 $cm^2\ V^{-1}\ s^{-1}$, respectively. In 2018, Hou *et al.* at the Institute of Chemistry, Chinese Academy of Sciences, first reported two NDI-type organic small molecules (NDI-N and NDI-Br) used as electron transport layer materials for organic solar cells (OSCs). Due to the high crystallinity and excellent film-forming properties of NDI-N, these materials exhibited superior electron transport performance and processability.[266]

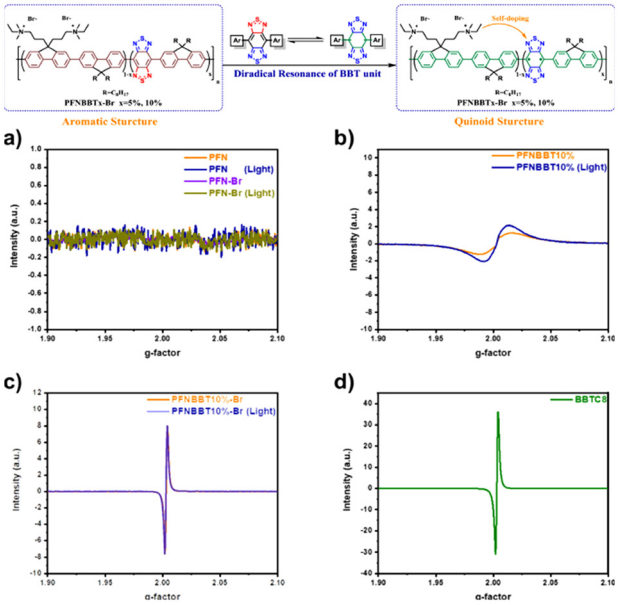

Fig. 11 The ESR spectra of the (a) PFN and PFN-Br, (b) PFNBBT, (c) PFNBBT10%-Br and (d) BBTC8.

Compared with NDI-based molecules, PDI-based molecules have also attracted significant attention as electron transport layer materials in OSCs. As early as 2014, the research teams led by Yongfang Li and Jizheng Wang at the Institute of Chemistry, Chinese Academy of Sciences, jointly reported two small-molecule electron transport layer materials based on PDI:PDIN and PDINO (Fig. 12). The only difference between the two compounds lay in their terminal substituents, with one containing a tertiary amine group and the other a tertiary

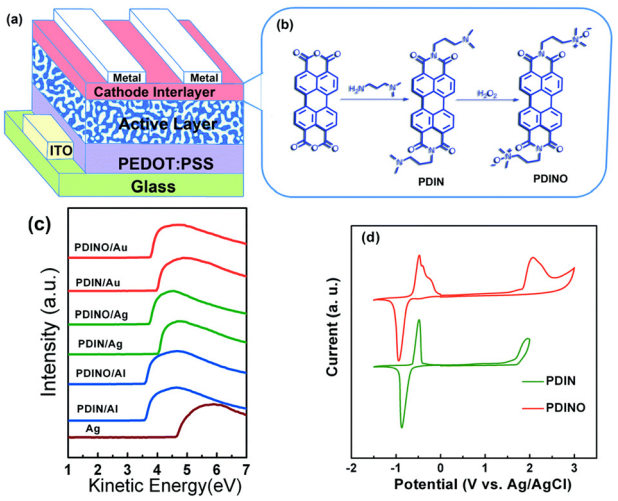

Fig. 12 (a) Device structure of the PSCs. (b) Synthetic route towards PDI-interlayers. Device parameters of the PSCs based on PTB7/$PC_{70}BM$ with PDI/Al as the cathode with various PDI thicknesses under the illumination of AM 1.5 G, 100 mW cm^{-2}. (c) UPS spectra of the PDI-interlayer treated electrodes. (d) Cyclic voltammograms of the PDIs.[123]

© 2025 The Author(s). Published by the Royal Society of Chemistry

Open Access Article. Published on 14 März 2025. Downloaded on 28.01.2026 01:53:57.
This article is licensed under a Creative Commons Attribution-NonCommercial 3.0 Unported Licence.

amine *N*-oxide. The inherently extended planar structure of the PDI unit enabled both materials to achieve a high electrical conductivity of 10^{-5} S cm^{-1}, exhibiting excellent capabilities in tuning the work function of the cathode.[123] Huang *et al.* synthesized two n-type WSCPs by incorporating NDI into traditional WSCPs (Fig. 13). Both WSCPs demonstrated good solubility in polar solvents and, due to the π-delocalized planar structure of the NDI unit with high electron affinity, exhibited high electron mobility and suitable energy levels. Additionally, the brominated quaternary ammonium polymer PNDIT-F3N-Br displayed significant self-doping behavior without requiring photoexcitation.[124]

2.3.5 Other electron-deficient units. In addition to NDI and PDI, several other electron-deficient units, such as benzothiadiazole (BT),[125,126] diketopyrrolopyrrole (DPP),[127,128] and isoindigo,[129,130] have been widely used in small molecules and polymers.[131] Compared with imide-functionalized polymers, polymers based on amide-functionalized (hetero)arenes, such as DPP, isoindigo (IID), and naphthalene diimide (NBA), generally exhibit p-type or ambipolar characteristics due to their higher frontier molecular orbital (FMO) levels (HOMO ~ −5.10 to −5.40 eV; LUMO ~ −3.50 to −3.90 eV). To further enhance electronic performance, the introduction of new electron-deficient building blocks and a deeper understanding of structure–property relationships are essential. For achieving n-type transport, electron-deficient units are typically incorporated to lower their energy levels.[132] Recently, benzodifuran-dione oligomers, based on electron-deficient conjugated backbones such as oligothiophene-benzodifurandione-vinylene (BFDO) materials, have demonstrated high electron mobility and excellent environmental stability.[110,112] BFDO, an electron-deficient unit, features four strong electron-withdrawing carbonyl groups embedded into the BDOPV backbone. This design results in a deep LUMO level of −4.24 eV, lower than many other electron-withdrawing units. The enlarged aromatic backbone of BDPPV not only extends the effective conjugation length, promoting intrachain transport, but also improves interchain transport due to the good planarity of the backbone. Furthermore, the strong electron-deficient building block BDOPV imparts lower HOMO/LUMO levels (−6.12/−4.10 eV) to BDPPV, resulting in high electron mobility up to 1.1 cm^2 V^{-1} s^{-1} under ambient conditions—four orders of magnitude higher than those of PPVs. BDPPV is the first polymer capable of transporting electrons over 1 cm^2 V^{-1} s^{-1} under ambient conditions, and its OFET devices exhibited good ambient stability for at least 30 days, maintaining an electron mobility of 0.31 cm^2 V^{-1} s^{-1}.[133] Through careful optimization of the polymerization reaction and doping process, researchers utilized the reversible redox properties of quinone-based oxidants to successfully accomplish the dehydrogenation polymerization of a benzodifuranone precursor. Notably, tetramethylbenzoquinone was used as the oxidizing agent, enabling the first successful oxidation-induced polymerization. As the degree of polymerization increased, the resulting polymer exhibited a significantly lower reduction energy level. Simultaneously, the generated tetramethylhydroquinone possessed a reducing ability, which enabled *in situ* n-type doping of the polymer, ultimately resulting in an n-type conductive polymer with a conductivity of up to 2000 S cm^{-1} (Fig. 14).[134]

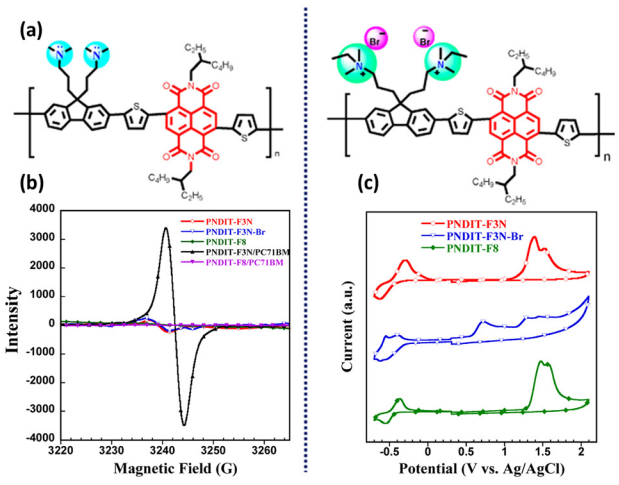

Fig. 13 (a) Chemical structures of PNDIT-F3N and PNDIT-F3N-Br. (b) ESR spectra of different polymers and blends in solid state. (c) Cyclic voltammograms of the polymers. Reprinted (adapted) with permission from ref. 124. Copyright 2016 American Chemical Society.

3. Applications

Conjugated polyelectrolytes (CPEs) have attracted significant attention in recent years due to their unique structural characteristics and diverse range of applications. By combining the exceptional electrical and optical properties of conjugated polymers with the ionic conductivity of polyelectrolytes, CPEs exhibit considerable potential in various fields, including photovoltaics, organic electrochemical transistors (OECTs), energy storage, and more.

3.1 Photovoltaics

The photovoltaic conversion process in organic solar cells (OSCs) is governed by a sequence of interdependent physical mechanisms. Initially, photon absorption within the photoactive layer induces electronic excitation from the highest occupied molecular orbital (HOMO) to the lowest unoccupied molecular orbital (LUMO) in either the donor or acceptor material, generating Frenkel excitons characterized by strong coulombic binding. These excitons require interfacial interactions for dissociation due to their inherently high binding energy. Subsequently, excitons diffuse across the active layer

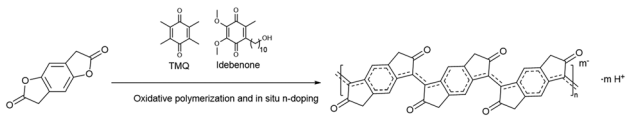

Fig. 14 Polymerization and doping process of PBFDO.

© 2025 The Author(s). Published by the Royal Society of Chemistry

Open Access Article. Published on 14 März 2025. Downloaded on 28.01.2026 01:53:57.
This article is licensed under a Creative Commons Attribution-NonCommercial 3.0 Unported Licence.

driven by concentration gradients; however, their short lifetime and the morphological constraints of phase-separated domains lead to partial quenching *via* radiative or non-radiative recombination, reducing photon-to-current efficiency. Upon reaching the donor–acceptor interface, charge transfer generates metastable charge-transfer (CT) excitons, where electrons and holes become spatially localized in the acceptor and donor materials, respectively, yet remain weakly coupled through residual coulombic interactions. The energy level offsets between donor and acceptor materials then drive the ultrafast dissociation of CT excitons into free charge carriers, achieving spatial separation of electrons and holes. Under the influence of the built-in electric field, liberated electrons migrate through the electron transport layer toward the cathode, while holes traverse the hole transport layer to the anode, culminating in photocurrent generation *via* electrode collection (Fig. 15). Critical factors determining device performance include interfacial energy alignment, optimized active layer morphology, and charge transport efficiency, which collectively govern the balance between exciton dissociation efficacy and recombination losses. This mechanistic framework underscores the importance of material design and device engineering in advancing OSC technologies.

The first OPV device was fabricated by Ching W. Tang in 1986, employing copper phthalocyanine as the donor and perylene tetracarboxylic derivative as the acceptor, achieving a PCE of 1%.[135] Although the relatively low PCE initially limited the development of OSCs, the introduction of bulk-heterojunction (BHJ) solar cells by Heeger *et al.* in 1995 marked a significant breakthrough. By blending a conjugated polymer donor and a fullerene acceptor in the active layer, the donor and acceptor undergo phase separation, forming bicontinuous interpenetrating networks at the nanoscale.[136] This morphology generates sufficient interfaces between the donor and acceptor, facilitating exciton dissociation and charge carrier transport, thus enhancing OSC performance. This discovery triggered extensive research on OSCs in both academia and industry.[137,138]

The PCE of OSCs is primarily determined by three key parameters: open-circuit voltage (V_{oc}), short-circuit current density (J_{sc}), and fill factor (FF). Significant research efforts have been devoted to identifying ideal donor and acceptor materials with well-matched energy levels to enhance OSC performance and improve charge injection efficiency.[38,139,140] In addition to optimizing the active layer, interface engineering plays a crucial role in improving both the performance and stability of OSCs. Given the strong coulombic interactions between holes and electrons in organic semiconductors, both geminate and non-geminate recombination occur during charge separation and transport, leading to notable PCE losses.[141]

The perovskite solar cell, an emerging technology, rivals crystalline silicon photovoltaics in laboratory efficiency while offering significant advantages in terms of cost and manufacturing processes.[142] Perovskite materials also exhibit excellent low-light performance and adjustable optoelectronic characteristics, attributes that crystalline silicon photovoltaics lack.[143] These advantages open up new possibilities for perovskite photovoltaics in various application scenarios, with the potential to bring photovoltaic technology into everyday household applications.[144–146] Perovskite materials typically display high light absorption and good charge mobility characteristics. Similar to organic solar cells, when light strikes the perovskite layer, excitons are generated, and the resulting electrons and holes are separated. Driven by an electric field, these charge carriers migrate toward the respective electrodes, generating electrical current. Despite impressive PCE exceeding 25%, PSCs still face significant challenges that prevent them from reaching their full commercial potential.[147] One of the key bottlenecks in enhancing the performance and stability of PSCs is the metal–oxide/perovskite interface, which plays a critical role in charge transport, recombination dynamics, and device longevity.[148] Metal–oxide charge-transport layers, typically used as electron and hole transport materials, often suffer from interface defects when in contact with perovskite materials. These defects lead to non-radiative recombination, reducing the efficiency of charge extraction and significantly lowering the overall performance of PSCs.[34,149,150]

Moreover, these interfaces are prone to undesirable chemical reactions during device operation, as well as mechanical delamination, which exacerbate the stability issues of PSCs. The defects at these interfaces can trap photogenerated charges, creating local electric fields that promote ion migration and phase separation, further degrading device performance over time.[152,153] Therefore, mitigating interface-related losses—such as non-radiative recombination, charge accumulation, and ion migration—becomes paramount to achieving both high efficiency and long-term stability in PSCs.[151]

In PSCs and OSCs, the active layer is typically positioned between the electron transport layer (ETL) and the hole transport layer (HTL). For efficient charge extraction, the conduction band minimum (E_c) of the active layer must be higher than that of the ETL, ensuring smooth electron flow from the active layer to the ETL. Likewise, the valence band maximum (E_v) of the active layer should be lower than that of the HTL to facilitate hole movement from the active layer to the HTL (Fig. 16). Ideally, the energy offset should not exceed 0.3 eV; otherwise, excessive offsets may impede charge transfer, increase energy loss, and potentially lead to recombination. Appropriate energy level alignment facilitates the transport of

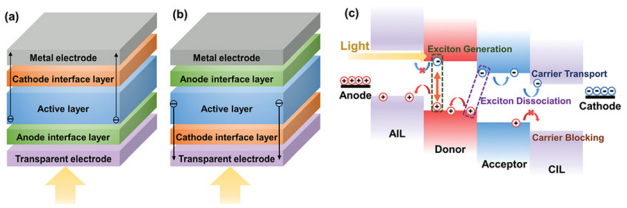

Fig. 15 The structure of single-junction OSCs and working mechanism illustration. OSC devices in (a) conventional structure or (b) inverted structure. (c) The working mechanism of carrier generation and transport in OSCs.[1]

© 2025 The Author(s). Published by the Royal Society of Chemistry

Open Access Article. Published on 14 März 2025. Downloaded on 28.01.2026 01:53:57.
This article is licensed under a Creative Commons Attribution-NonCommercial 3.0 Unported Licence.

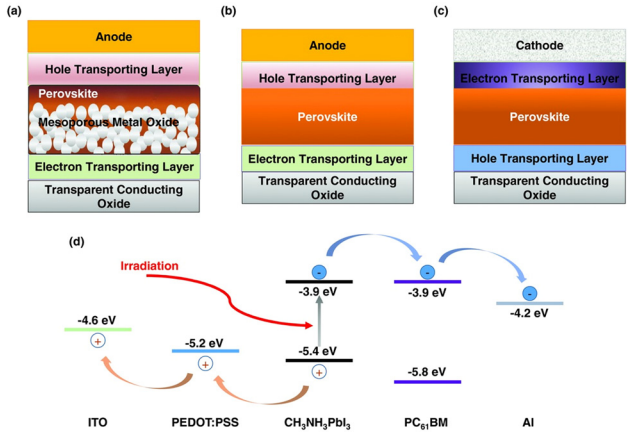

Fig. 16 (a) Schematic diagram of regular mesoporous structure, (b) schematic diagram of regular planar structure, (c) schematic diagram of inverted planar structure, (d) schematic diagram of the working principle in the inverted Pero-SC.[151]

unipolar charge carriers, ensuring efficient extraction and transfer of photogenerated charges while minimizing carrier recombination losses. Additionally, selecting appropriate interfacial materials can establish built-in electric fields that enhance the driving force for charge separation.

At the interface, charge extraction, transfer, and recombination are critical processes influencing photovoltaic performance. Rapid interfacial charge transfer promotes efficient extraction of photogenerated current, thereby enhancing the overall efficiency of the device. High mobility in the ETL and HTL optimizes charge dynamics at the interface, further reducing charge losses. On the other hand, deep defects at the interface can induce carrier recombination, leading to losses in V_{oc}. Therefore, minimizing interfacial recombination is essential for enhancing V_{oc} and overall device performance.[1,154]

Interface engineering serves as an effective and straightforward method to optimize interfacial properties, addressing interfacial losses without compromising the characteristics of the bulk layer. When designing interfacial materials, it is crucial to consider not only the stability of these materials but also their impact on the active layer. Preventing degradation at both the interface and the active layer is essential to maintaining long-term device performance. Furthermore, optimizing the interface can protect the entire device from degradation, significantly enhancing its stability. In conclusion, interface engineering plays a crucial role in optimizing the structure and properties of the interface layers, thereby enhancing the performance of thin-film devices.[111]

3.1.1 Anode engineering. An ideal anode interfacial layer (AIL) should facilitate hole extraction while inhibiting electron collection. It must possess an appropriate work function, neutral pH, high transmittance, and ease of processing, thereby maximizing the efficiency of both OSCs and PSCs.[143] Materials for the HTL should meet several criteria: (i) a high work function that matches the HOMO energy level of the donor material and the anode, (ii) transparency to enhance light absorption in the active layer, (iii) high hole mobility to minimize charge accumulation and recombination, (iv) a large bandgap to block electron carriers, and (v) chemical stability to withstand external factors.[1,156] Inorganic anode interfacial layers, such as MoO_3, copper oxide (CuO_x), and NiO_x, typically require thermal decomposition for fabrication, which is an expensive and vacuum deposition-intensive process. In comparison, organic materials offer advantages like lower cost, minimal toxicity, simpler solution processing, and a high work function, making them more suitable for industrial-scale fabrication. PEDOT:PSS has been the most widely used organic HTL due to these advantages. Over the past few decades, OSCs and PSCs incorporating PEDOT:PSS as the AIL have achieved remarkable power conversion efficiency (PCE) records, surpassing 20% and 27%, respectively.[157,158] However, its acidity can compromise device stability. Therefore, developing hole transport materials that offer high mobility, long-term stability, and comprehensive passivation is crucial for future advancements. For instance, CPE-K, when compared with PEDOT:PSS, does not induce electrode corrosion.[159] Moreover, the self-doping effect of CPE-K, as demonstrated by absorption spectrum and electron spin resonance (ESR) testing, enhances its conductivity to 1.5×10^{-3} S cm^{-1}, reducing charge recombination at the anode/active layer interface. As a result, CPE-K-based OSCs show slightly enhanced J_{sc} and PCE compared with those with PEDOT:PSS.[160,161]

The use of self-assembled monolayers (SAMs) as HTLs significantly reduces charge transport losses, thereby enhancing J_{sc} and V_{oc} in PSCs. SAMs, designed with one anchoring group and one functional group, adhere easily to surfaces and can modulate the properties of perovskite layers.[163] This approach has led to record-high PCEs and impressive stability in single-junction devices.[21,164–166] Additionally, the integration of SAMs in tandem and flexible PSCs facilitates the fabrication of large-area devices. For example, the addition of small molecule 2PACz into the active layer leads to spontaneous self-organization during film formation. The vertical migration of 2PACz in the bulk heterojunction (BHJ) is driven by its higher surface energy, which directs it towards the ITO substrate. This process reduces surface trap density and improves device performance, achieving a remarkable PCE of 15.8% in large-area OSCs processed with green solvents (Fig. 17). Furthermore, self-assembled 2PACz SAMs have shown potential in enhancing the stability and performance of BHJ-OPVs, where their direct functionalization of ITO increases the work function and reduces contact resistance, significantly improving device stability (Fig. 18).[155,162]

In PSCs, the self-assembly of hole transport molecules on NiO nanocrystalline films has led to a certified PCE of 24.4%, demonstrating the effectiveness of SAMs in improving energy level alignment, reducing interfacial recombination, and enhancing hole extraction.[159] Poly-4PACz, a novel hole transport material designed through the polymerization of carbazole phosphonic acid small molecules, offers several advantages over traditional small-molecule HTMs. Unlike the

© 2025 The Author(s). Published by the Royal Society of Chemistry

Open Access Article. Published on 14 März 2025. Downloaded on 28.01.2026 01:53:57.
This article is licensed under a Creative Commons Attribution-NonCommercial 3.0 Unported Licence.

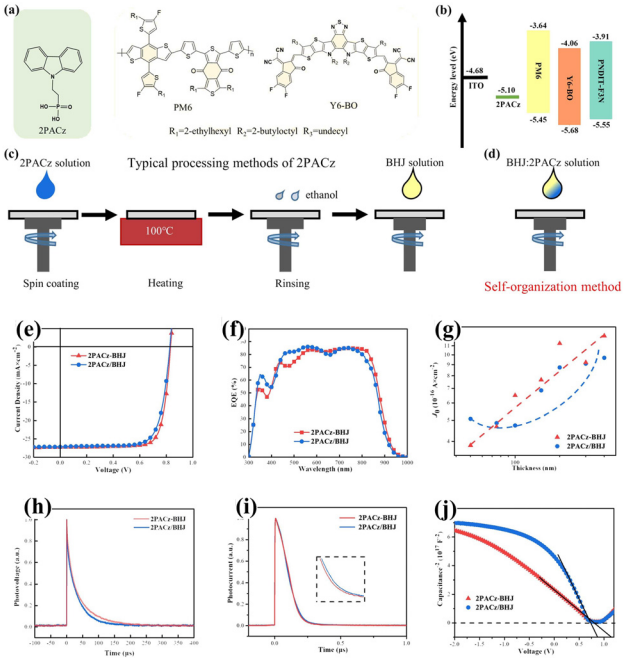

Fig. 17 (a) Molecular structures of BHJ materials and 2PACz. (b) Energy level diagram of key materials in device. (c) 2PACz fabrication procedures of the independent spin-coating method. (d) Fabrication procedures of the self-organization method. (e) Current density–voltage (J–V) characteristics. (f) External quantum efficiency spectra. (g) The dependences of saturation current density J_0 on thickness of 2PACz–BHJ (red dots) and 2PACz/BHJ devices (blue dots). (h) Normalized transient photovoltage traces of devices. (i) Normalized transient photocurrent traces of devices. (j) Mott–Schottky curves of OSCs based on ITO/2PACz/BHJ and ITO/2PACz-BHJ devices.[155]

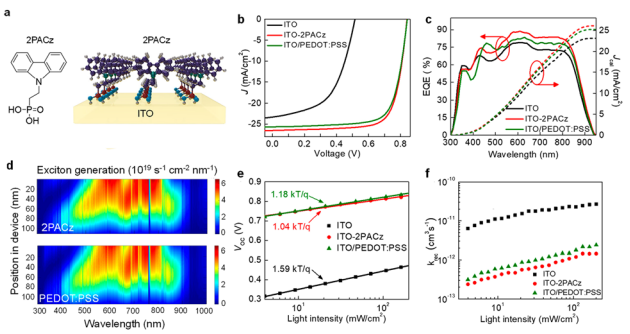

Fig. 18 (a) Chemical structure of 2PACz and schematic illustration of the ITO-2PACz electrode. (b) J–V curves of PM6:N3 solar cells based on ITO, ITO-2PACz, and ITO/PEDOT:PSS. (c) External quantum efficiency (EQE) curves of the same OPV. (d) Optical simulations for the exciton generation rate profiles in the studied SAM and PEDOT:PSS-based OPV devices. Light intensity dependence of (e) V_{oc} and (f) bimolecular recombination rate constant (k_{rec}) for the same cells.[162]

compact ultrathin SAMs required by PACz-HTM, Poly-4PACz exhibits good electrical conductivity, which makes it less sensitive to layer thickness and the roughness of transparent conductive oxides (TCOs) (Fig. 19). This significantly broadens the processing window for HTMs. Additionally, the phosphonic

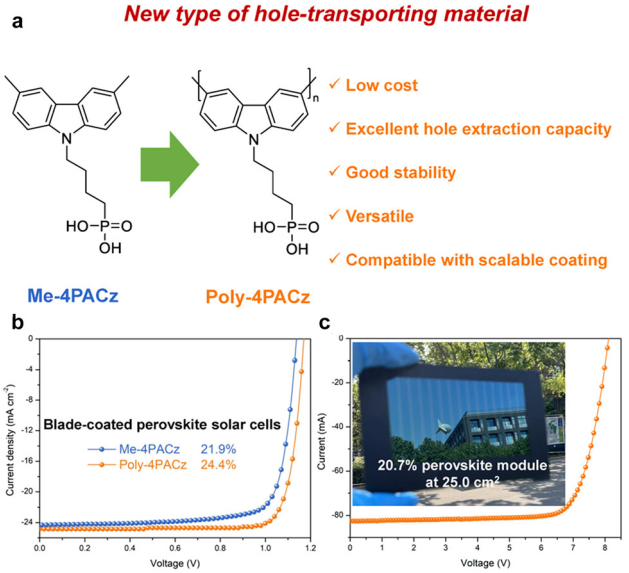

Fig. 19 (a) Molecular structure of Me-4PACz and Poly-4PACz. (b) J–V curves of the blade-coated PSCs based on Me-4PACz and Poly-4PACz. (c) J–V characteristics of the Poly-4PACz-based perovskite mini-module with an aperture area of 25.0 cm^2. Inset shows a picture of Poly-4PACz-based perovskite module.

acid groups in Poly-4PACz form strong chemical bonds with TCOs and passivate the perovskite film, suppressing charge recombination at the buried perovskite/HTM interface. This material represents a promising direction for enhancing the performance and stability of PSCs and OSCs (Table 1).[20]

3.1.2 Cathode engineering. The primary function of cathode interfacial layers (CILs) is to facilitate efficient electron transport while blocking holes, ensuring a good contact between the active layer and electrodes, and reducing the electrode work function effectively.[1,171] Ideal cathode interlayer materials (CIMs) should possess tunable work function (WF), high conductivity, stability, and favorable interfacial contact.[147–149] A series of water- and alcohol-soluble conjugated polymers and/or small molecules have been developed, significantly enhancing device performance in PSCs and organic photovoltaics (OPVs). These CILs feature solubility in environmentally friendly solvents such as water and alcohol, which enables their use in the fabrication of multilayer devices without causing layer corrosion. Moreover, these materials improve interfacial contact between the active layer and the cathode, thereby boosting photovoltaic efficiency (Table 2).[3]

Table 1 Different types of SAMs and their device performance

	V_{oc} (V)	J_{sc} (MA cm^{-2})	FF (%)	PCE (%)	Ref.
MeO-4PACz	1.15	24.53	84.56	24.5	167
2PACz	1.186	25.78	80.8	23.4	168
DC-TMPS	1.18	25.0	84.0	24.8	169
MeO-2PACz	1.18	23.68	83.21	23.31	170
Poly-4PACz	1.17	24.8	83.9	24.4	20

© 2025 The Author(s). Published by the Royal Society of Chemistry

Open Access Article. Published on 14 März 2025. Downloaded on 28.01.2026 01:53:57.
This article is licensed under a Creative Commons Attribution-NonCommercial 3.0 Unported Licence.

Table 2 The work function (WF) of Ag electrodes modified by 5 nm CPEs and the electron mobility of these CPEs

	V_{oc} (V)	J_{sc} (MA cm^{-2})	FF (%)	PCE (%)	Ref.
PFNBBT10%-Br	0.82	27.59	71.27	16.35	182
PFBP-Br	0.83	26.12	73.49	16.2	183
DPTFBr	0.84	26.23	73.27	16.14	183
PDINN	0.913	26.9	78.25	19.19	184
NDI-PhC4	0.855	27.7	80.7	19.1	185

In 2012, Wu *et al.* introduced PFN as a CIL material, achieving a power conversion efficiency (PCE) of 8.24% in inverted OSCs. The performance was further enhanced to 9.21% in inverted devices based on PTB7:PC71BM. PFN was found to lower the work function of indium tin oxide (ITO) from 4.7 eV to 4.1 eV, facilitating efficient electron extraction and improving device efficiency.[172,173] Luo *et al.* utilized water/alcohol-soluble polyelectrolytes such as PFPNBr and PFNBr-DBT15 as CILs, demonstrating that the insertion of a thin layer of WSCP induced an interfacial dipole, enhancing the built-in potential and increasing the V_{oc} by up to 0.3 V.[174] While PFN-like materials show promising performance, challenges remain, including low charge mobility (approximately 1×10^{-6} to 1×10^{-7} cm^2 V^{-1} S^{-1}), which limits the optimal thickness of these interlayers to around 10 nm. Even small increases in thickness can significantly degrade device performance.[175] To overcome these limitations, interface materials with higher charge mobility and conductivity have been developed by enhancing molecular packing and introducing molecular doping, particularly using planar units such as NDI and PDI.[176–180] These advanced materials exhibit thickness-insensitive behavior, ensuring optimal performance across a wide range of thicknesses.[23] For instance, Huang *et al.* designed and synthesized three self-doped n-type water-soluble conjugated polymers (n-WSCPs) based on perylenetetracarboxylic acid derivatives: PIF-PTE-N, PIF-PMIDE-N, and PIF-PDI-N. The distinct electron-deficient units in their backbones provided tunable absorption properties and adjustable energy levels. Using ultrathin n-WSCPs as electron transport layers (ETLs), high-performance PSCs with PCEs near 9% were achieved, with PIF-PDI-N-based devices maintaining PCEs over 9% even at 50 nm thickness, suggesting potential for large-area fabrication *via* roll-to-roll processing. In contrast, devices based on PIF-PTE-N and PIF-PMIDE-N underperformed due to mismatched energy levels and insufficient electron mobility.[181] Li *et al.* reported a series of NDI-based conjugated polyelectrolytes as universal, thickness-insensitive ETMs for OSCs. Substituting the conjugated backbone with alkyl and alkoxy ammonium side chains altered the absorption spectra, energy levels, and doping behavior, achieving PSCs with PCEs exceeding 16% when PM6:Y6 was used as the active layer (Fig. 20).[122]

In addition to introducing electron-deficient units like NDI, incorporating electron-deficient atoms such as fluorine has proved effective in enhancing the performance of CPEs.[186,187] Liu *et al.* developed fluorinated CPEs as electron transport layers for inverted solar cells, finding that fluorine content significantly affected the interfacial dipole, conductivity, and morphology of the active layer. The highest fluorine content in PFf4B resulted in significantly higher efficiency and allowed for thicker films (~31.8 nm).[188] Li *et al.* further optimized CPE properties by tuning counterions such as F$^-$, Cl$^-$, BIm$_4^-$, and BArF$_4^-$, which affected the doping process and electron mobility (Fig. 21). CPEs with optimized counterions demonstrated improved performance, making them promising candidates for large-area PSC fabrication.[189]

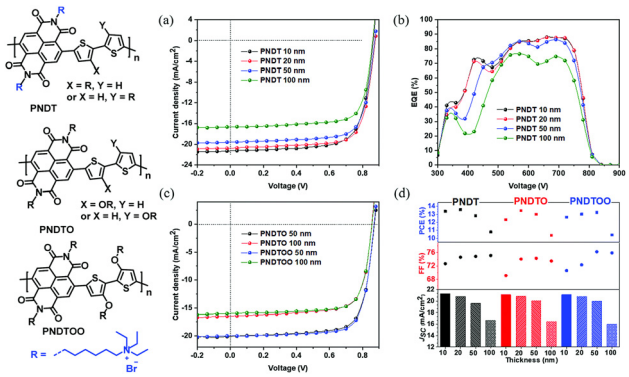

Fig. 20 *J–V* characteristics (a) and (b) the EQE curves of PBDB-2Cl:ITIC-2F-based photovoltaic devices with PNDT as the ETM; (c) *J–V* characteristics of PBDB-2Cl:ITIC-2F-based photovoltaic devices with PNDTO and PNDTOO as ETMs; and (d) the summary of photovoltaic parameters for PBDB-2Cl:ITIC-2F-based photovoltaic devices with these CPEs as ETMs.[122]

Moreover, similar to alkylamines in polymer-based ETLs, which enhance the ETL/cathode interface through better work function matching, the use of such materials also improves the perovskite/ETL interface by effective trap passivation Table 3. This reduces defect density and charge recombination, further improving PSC performance (Table 4).[146,177,190]

3.2 Transistors

With the rapid advancement of flexible electronics, sensors, and bioelectronic devices, organic transistors have emerged as a prominent research focus in recent years, owing to their unique material properties and wide-ranging application potential.[191] Among these, organic electrochemical transistors (OECTs) stand out as particularly representative devices.[8,192,193] OECTs offer advantages such as high transconductance, excel-

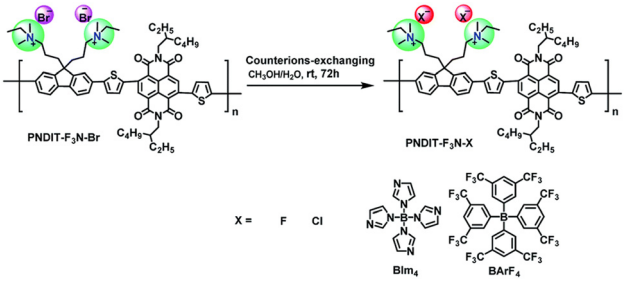

Fig. 21 Chemical structure of PNDIT-F$_3$N-X.

© 2025 The Author(s). Published by the Royal Society of Chemistry

Open Access Article. Published on 14 März 2025. Downloaded on 28.01.2026 01:53:57.
This article is licensed under a Creative Commons Attribution-NonCommercial 3.0 Unported Licence.

Table 3 The work function (WF) of Ag electrodes modified by 5 nm CPEs and the electron mobility of these CPEs

	PNDIT-F_3N-F	PNDIT-F_3N-Cl	PNDIT-F_3N-Br	PNDIT-F_3N-BIm_4	PNDIT-F_3N-$BArF_4$
WF of Ag (eV)	4.08	4.08	3.99	4.13	5.63
Electron mobility ($\times 10^{-4}$ cm^2 V^{-1} s^{-1})	1.45	2.91	3.78	2.35	0.0012

lent biocompatibility, low operating voltage, and minimal power consumption.[78,194–196] These benefits are closely tied to the transistor's unique operating principle, wherein the gate voltage (V_G) drives ions from the electrolyte into the channel, resulting in volumetric doping and de-doping of the organic semiconductor. This mechanism enables OECTs to demonstrate remarkable performance in applications such as sensors, medical devices, and display technologies.[78,194–196] In OECTs, conductivity is controlled through electrochemical interactions between electrolytes and organic semiconductors.[197] An OECT typically consists of a thin organic semiconductor film in contact with an electrolyte, with a gate electrode immersed in the electrolyte. Metal source and drain electrodes establish contact with the organic semiconductor, defining the channel through which holes or electrons flow between the source and drain (Fig. 22). The operation of the OECT relies on ion injection from the electrolyte into the organic semiconductor, altering its doping state and thereby modulating its conductivity. This process is described using terminology from both electrochemistry and solid-state physics, with control provided by the gate voltage (V_G) and drain voltage (V_D), referenced to the source electrode.[194] The gate voltage modulates ion injection into the channel, regulating the doping state (or redox state, in electrochemical terms) of the organic film, while the drain voltage generates a current (I_D), which is proportional to the charge carriers (holes or electrons) moving through the channel, reflecting the doping state of the organic film. Like MOSFETs and OFETs, OECTs can function as switches, where the gate voltage (input) controls the drain current (output). Additionally, they can act as amplifiers, where the input signal is amplified during the output process.[194] OECTs are capable of converting small voltage signals applied to the gate into significant changes in the drain current. The transduction efficiency is quantified by the first derivative of the transfer curve, known as transconductance ($gm = \partial I_D/\partial V_G$), a critical figure of merit for transistors. OECTs typically exhibit exceptionally high transconductance values in the millisiemens range, even for micrometer-scale devices.[194,198]

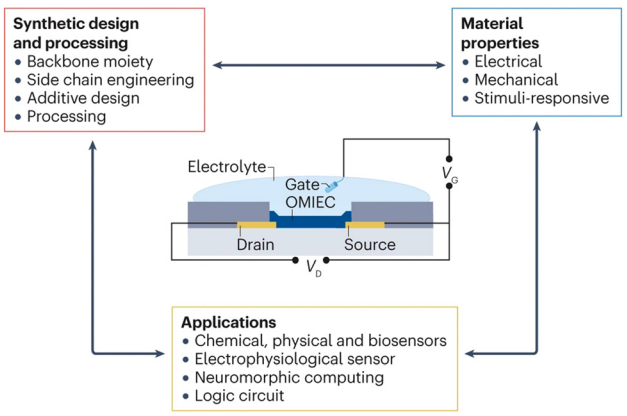

Fig. 22 The synthetic design controls the properties of organic mixed ionic–electronic conductors (OMIECs), which enable particular applications.[31]

For optimal performance, the channel material must effectively conduct both ionic and electronic signals. Commonly used materials include PEDOT:PSS and other CPEs. Due to its high conductivity and solution processability, PEDOT has become widely used in thin-film devices.[199–201] However, the water solubility of PEDOT necessitates the incorporation of crosslinking agents, such as (3-glycidyloxypropyl)trimethoxysilane and divinylsulfone, to render it water-insoluble.[201,202] While PEDOT is relatively straightforward to use in OECTs, devices based on PEDOT typically operate in depletion mode, which may limit long-term device stability.[199] In the absence of a gate voltage, with only a bias applied between the source and drain electrodes, the PEDOT remains in its conductive state. This is because the negatively charged PSS compensates for the positive charges in PEDOT, maintaining a high hole density in the material. When a positive bias is applied to the gate electrode, positive ions from the electrolyte migrate toward the active layer and infiltrate the polymer network. These ions neutralize the negative charges on PSS, leading to a reduction in hole density (de-doping) and causing the device to transition from "on" to "off" state.[24] Scott *et al.* demonstrated that to shift PEDOT:PSS OECTs into enhancement-mode, charge-compensating sulfonate units on the PSS component must be neutralized by electron donation to the PEDOT backbone.[200] This can be achieved using amines as dedoping agents, where the amine groups of PEI transfer electrons to PEDOT, significantly reducing the intrinsic conductivity of the channel and enabling accumulation-mode operation.[200] Additionally, the bulky structure of PSS affects the volumetric capacitance of the PEDOT film by influencing the fraction of PEDOT in the film.[203] As such, the development of novel single-component ion–electron mixed-conducting CPEs has become a key area of focus.

In this context, CPEs such as PTHS were developed. The sulfonic acid groups in PTHS are directly attached to the thiophene backbone *via* side chains, creating a conjugated polyelectrolyte with distinct electrical properties. When the counterions are compensated by electronic charges, the material becomes conductive, whereas it behaves as an insulator when ion-compensated.[204] Bazan *et al.* utilized a self-doped CPE-K to fabricate high transconductance accumulation-mode

Open Access Article. Published on 14 März 2025. Downloaded on 28.01.2026 01:53:57. This article is licensed under a Creative Commons Attribution-NonCommercial 3.0 Unported Licence.

Table 4 Device data of PSCs based on NT812/$PC_{71}BM$ with 5 nm CPEs as the ETMs

	V_{oc} (V)	J_{sc} (MA cm^{-2})	FF (%)	PCE (%)
No ETM	0.65 ± 0.01	17.91 ± 0.31	63.77 ± 1.79	7.45 ± 0.09 (7.55)a
PNDTT-F_3N-F	0.73 ± 0.00	19.19 ± 0.21	69.15 ± 0.92	9.62 ± 0.07 (9.71)
PNDIT-F_3N-Cl	0.73 ± 0.00	19.53 ± 0.23	70.99 ± 0.33	10.16 ± 0.14 (10.26)
PNDTT-F_3N-Br	0.73 ± 0.00	19.55 ± 0.22	72.18 ± 1.03	10.32 ± 0.15 (10.50)
PNDIT-F_3N-BIm4	0.73 ± 0.00	19.56 ± 0.23	71.12 ± 0.38	10.14 ± 0.11 (10.23)
PNDIT-F_3N-BArF4	0.53 ± 0.00	17.84 ± 0.41	45.22 ± 2.44	4.25 ± 0.30 (4.49)

OECTs. The direct cross-linking of GOPS to the sulfonate functional group on CPE-K was confirmed by XPS. OECT devices based on CPE-K exhibited accumulation-mode operation, offering advantages such as low power consumption when the device is in the "off" state. The transconductance of these devices was compared with other OECT materials from the literature, considering factors such as channel volume and operational voltage.[205] However, due to the water solubility of CPEs, crosslinking agents are required to stabilize the thin films, although their inclusion dilutes the active material in the transistor channel. Despite enhancing water stability, this approach compromises the mixed ionic–electronic conductivity.[206–208] To address this limitation, Philip *et al.* introduced hydrophobic copolymer monomers (*e.g.*, P3HT) into PTHS *via* copolymerization, reducing the polymer's water solubility by 50%. This modification effectively decreases the need for crosslinking agents while maintaining high ionic conductivity within the copolymer structure.[206]

OECTs have shown promise in a wide range of applications, including biosensors, flexible electronics, and wearable technology, owing to their high conductivity and tunable properties. These devices are particularly suited for real-time monitoring of biological signals, such as ions, electrophysiological signals, and biomarkers, contributing to advancements in healthcare.[9,106,209–211] Additionally, the low cost and ease of fabrication make OECTs an attractive option for large-scale production of flexible displays and smart materials. Biologically significant ions, such as K^+, Na^+, and Ca^{2+}, play crucial roles in physiological processes. In particular, K^+ and Na^+ are essential for nerve impulse transmission, muscle contraction, and maintaining water balance across cell membranes.[193,212] Li *et al.* explored the use of [MTEOA][$MeOSO_3$] as an additive to enhance the conductivity of PEDOT, improving the performance of OECTs. Devices fabricated with PEDOT/[MTEOA][$MeOSO_3$] films as the active layer exhibited high transconductance (22.3 ± 4.5 mS μm^{-1}), a substantial μC^* product (283.80 ± 29.66 F cm^{-1} V^{-1} s^{-1}), and rapid response times (~40.57 μs). Furthermore, the devices demonstrated excellent cyclical stability, retaining 95% of their performance after 5000 switching cycles. Ion sensors based on these PEDOT/[MTEOA][$MeOSO_3$]-integrated OECTs, combined with ion-selective membranes, exhibited high sensitivity and selectivity for detecting Na^+ and K^+, showcasing their potential in monitoring physiological ion concentrations and human vital signs.[213] Bai *et al.* proposed a wearable glucose sensor based on an OECT for continuous glucose monitoring (CGM). Compared with traditional electrochemical sensing-based CGM systems, the OECT-CGM offers improved noise resistance and adjustable sensitivity, making it a promising solution for monitoring glucose levels both *in vitro* and *in vivo*.[209]

Despite these advances, the development of complementary logic circuits based on OECTs remains hindered by the limited variety and performance of n-type materials compared with p-type materials.[214,215] Currently, air-stable n-channel materials are constructed by developing electron-deficient building blocks, such as perylenediimides (PDI),[215,216] naphthalenediimides (NDI),[215,217] diketopyrrolopyrrole (DPP),[129,218] and isoindigo (IID).[215] Giovannitti *et al.* reported a series of donor–acceptor random copolymers with an NDI core. Among the seven copolymers, P-90 demonstrated the best performance, with a conductivity of 0.21 S cm^{-1} and an electron mobility of 2.38 × 10^{-4} cm^2 V^{-1} s^{-1}.[219] They also investigated the effect of side chains on device performance, finding that alkyl side chains favored electron transport, while glycol side chains favored ion conduction. The relative ratio of side chains modulated the balance between ionic and electronic conduction, enhancing the performance of OECTs.

3.3 Energy storage

The growing global population has led to an increasing demand for energy. While fossil fuel combustion has historically been the primary source of energy, it is associated with significant environmental challenges, including the release of greenhouse gases. As awareness of these detrimental effects grows, there has been a substantial shift toward renewable energy sources such as solar, wind, hydro, and geothermal power. Despite rapid advancements in renewable energy technologies, their intermittent nature presents a substantial challenge. This has driven a focus not only on energy conversion but also on energy storage. In response to this challenge, various energy storage technologies have emerged, with electrochemical energy storage being particularly promising.

Lithium-ion batteries (LIBs) have become the dominant energy storage technology for applications ranging from consumer electronics and portable devices to electric vehicles (EVs), plug-in hybrid electric vehicles (PHEVs), and even military and aerospace systems.[220,221] Their popularity stems from their high energy and power density, long cycle life, and relatively lightweight design. Developed in the 1970s and commercialized by Sony in 1990, LIBs have undergone significant improvements, revolutionizing industries such as electronics

 © 2025 The Author(s). Published by the Royal Society of Chemistry

Open Access Article. Published on 14 März 2025. Downloaded on 28.01.2026 01:53:57.
This article is licensed under a Creative Commons Attribution-NonCommercial 3.0 Unported Licence.

and transportation.[6,222] However, despite their widespread use, LIBs face challenges related to the mechanical and chemical stability of electrode materials. Innovations in binder systems, particularly those involving conductive polymers, are being explored to enhance performance, durability, and energy density, which could help address issues such as mechanical degradation and energy inefficiency.

A LIB operates by the intercalation and deintercalation of lithium ions between the cathode and anode during charging and discharging. As shown in Fig. 23, the working principle involves electrochemical reactions: during charging, an applied voltage causes lithium ions (Li^+) to deintercalate from the cathode material, migrate through the electrolyte, and intercalate into the anode (usually graphite). At the same time, electrons released from the cathode flow through an external circuit to the anode, maintaining charge balance. During discharge, lithium ions deintercalate from the anode, pass through the electrolyte, and return to the cathode, while electrons travel through the external circuit from the anode to the cathode, powering external devices.

The performance of LIBs is influenced not only by the anode and cathode materials but also by auxiliary materials such as conductive agents and binders. These components play a critical role in enhancing the conductivity, structural stability, and electrochemical performance of the battery.

3.3.1 Conductive agents for anodes and cathodes. Conductive agents, typically carbon-based materials such as acetylene black, carbon nanotubes (CNTs), and graphene, are essential for improving electron conduction within electrode materials. They help reduce internal resistance and ensure the effective reaction of lithium ions during the charge and discharge cycles. The use of conductive agents is particularly important for certain cathode materials, such as lithium iron phosphate ($LiFePO_4$), which exhibit relatively poor conductivity.[224] Graphite, commonly used in anodes due to its excellent conductivity, also requires the addition of conductive agents to ensure uniform electron distribution throughout the electrode.[225,226]

Binders are used to bond active materials and conductive agents to the current collectors, ensuring the mechanical integrity and structural stability of the electrodes. Common binders include polyvinylidene fluoride (PVDF) and carboxymethyl cellulose (CMC).[7,227] PVDF is widely used for cathodes due to its chemical stability and electrochemical inertness, which helps maintain electrode stability. In anode materials, a combination of water-soluble binders, such as CMC, and styrene–butadiene rubber (SBR) is often used. This combination not only reduces battery resistance but also provides environmental benefits. Although binders and conductive agents do not directly participate in the insertion/extraction of lithium ions, they are crucial for the overall performance of the battery. Their appropriate selection and optimization are vital for enhancing the electrochemical performance of LIBs, especially with regard to cycling stability and rate capability. Despite PVDF's widespread use as a binder, it has significant drawbacks, including poor electronic and ionic conductivity.[228] This has prompted the development of conductive polymer electrolytes, which possess both ionic and electronic conductivity, as potential alternatives to traditional binders.

One of the first electrode materials to be industrialized for LIBs was lithium iron phosphate ($LiFePO_4$), known for its olivine structure. LFP is favored for its excellent thermal stability, cost-effectiveness, safety, and minimal environmental impact. However, its application in high-rate environments is limited by its poor electronic conductivity (10^{-9} to 10^{-10} S cm^{-1}) and the presence of one-dimensional lithium ion (Li^+) channels. The integration of conductive polymer binders has proved to be an effective strategy for improving electronic conductivity and stabilizing the solid electrolyte interphase (SEI) at the electrodes.[229] For example, Li *et al.* introduced a water-soluble binder that significantly enhances the bond strength of the anode compared with traditional commercial PVDF binders. The binder, TA, characterized by its reactive –OH groups and dendritic ring structure, facilitates hydrogen bonding with $–SO_3H$ in PEDOT:PSS, forming a cohesive network structure that demonstrates exceptional rate capability and long-term stability over 1000 cycles.[186] S. N. Eliseeva *et al.* prepared a lithium-ion battery without the addition of conductive carbon black. By employing polymer dispersion PEDOT:PSS along with CMC as an additive to C-LFP-based cathode material, the specific capacity and C-rate performance of the electrodes were significantly improved compared with conventional C-LFP/PVDF electrodes. This improvement was primarily due to the increased active mass of LFP from 84% to 96%, leading to a 13% increase in specific capacity, reaching 148 mA h g^{-1}.[230] In addition to PEDOT:PSS, many other CPEs have been utilized to develop novel binders for LIBs.[192,231,232] For instance, Yo Han Kwon *et al.* introduced poly[3-(potassium-4-butanoate) thiophene] (PPBT), a water-soluble, carboxylate-substituted polythiophene, as a binder component. The introduction of PPBT as a binder and polyethylene glycol (PEG) as a surface coating on the Fe_3O_4 active particle surface demonstrated significant improvements in both electron and ion transport. This combination reduced electrode resistance, stabilized cycling performance, and improved rate capability (Fig. 24).[5]

Apart from binder in LIBs, CPEs were also utilized in Li metal batteries (LMBs).[233–235] When PEDOT is used as a binder, its high conductivity can significantly enhance the

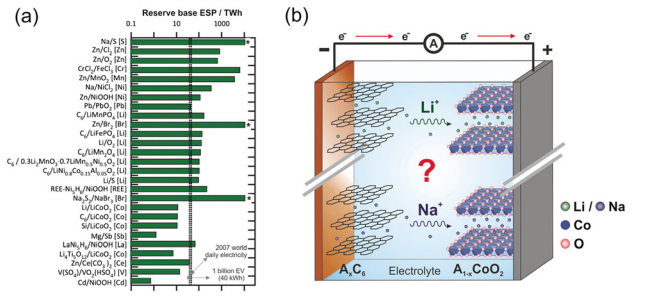

Fig. 23 (a) Energy storage potential in TWh for different battery chemistries. The limiting element by resource constraints is shown in brackets. The star indicates that the ESP value is beyond the limit of the Figure. (b) Sketch of the well-known working principle of a lithium-ion battery (LIB) with lithium ions intercalating into two host structures.[223]

Open Access Article. Published on 14 März 2025. Downloaded on 28.01.2026 01:53:57.
This article is licensed under a Creative Commons Attribution-NonCommercial 3.0 Unported Licence.

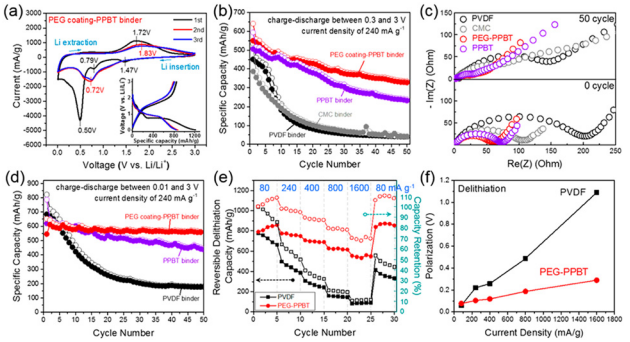

Fig. 24 Electrochemical performance of Fe_3O_4-based electrodes. (a) CV profiles of PEG-Fe_3O_4/carbon/PPBT electrode in the potential window of 0.01 to 3 V *versus* Li/Li$^+$ collected at the rate of 0.5 mV s^{-1} (the inset shows the galvanostatic charge–discharge profiles in the potential window of 0.01 to 3 V *versus* Li/Li$^+$ at a constant current density of 80 mA g^{-1}, comparable to CV profiles). (b) Cycling performance (=capacity retention as a function of cycle number) collected for the current density of 240 mA g^{-1} (~0.3 C) between 0.3 and 3 V (open circles: Li-insertion capacity, filled circles: Li-extraction capacity). (c) The impedance spectra measured at 3 V before cycling (bottom graph) and at open-circuit voltage (OCV) after 50 cycles (upper graph) in the frequency range from 1 MHz to 0.1 Hz. (d) Cycling performance between 0.01 and 3 V. (e) Delithiation rate capability, where cells were lithiated at a constant current density of 80 mA g^{-1} and delithiated at different current densities between 0.01 and 3 V (open symbols: capacity retention, filled symbols: Li-extraction capacity). (f) Cell polarization as a function of the applied current density during the delithiation process.[5]

electron transfer capability between the cathode active materials. In addition, the cross-linked network structure of PEDOT can accommodate the volume changes of the cathode during the discharge/charge cycles. Incorporating the conductive polymer PEDOT as a binder in the cathode of lithium–sulfur batteries, in conjunction with hollow porous carbon particle hosts, effectively mitigates the polysulfide shuttle effect, enhances lithium-ion migration, and ultimately elevates the overall battery performance. Experimental data and predictions of multiscale simulations concluded a 7–9% extension of the specific capacity of Li–S battery cells due to the surface redox effect of PEDOT:PSS and elimination of lithium sulfides from the anode by slowing down their migration and shuttling *via* their adsorption by the PEDOT:PSS binder.[236] In addition to changes in electrode materials, researchers are also focusing on solving the polysulfide shuttle issue in lithium–sulfur batteries through separator modification. Due to the difference in charge between lithium ions and polysulfide anions, the use of an ion-selective membrane is an effective solution to the polysulfide shuttle issue.[237] The sulfonated tetrafluoroethylene-based fluoropolymer copolymer, commonly known as Nafion, is a typical polymer that can be utilized as a coating to create a permselective membrane. When applied to the separator, Nafion allows the selective diffusion of Li$^+$ cations while blocking the movement of polysulfide anions, owing to its electronegative SO_3^- groups. This selective ion transport significantly enhances the electrochemical performance of Li/S batteries.[237–241] Due to the abundant sulfonic acid groups and excellent conductivity of PEDOT:PSS, Wang *et al.* deposited a highly conductive and lightweight PEDOT:PSS interlayer onto the separator. This interlayer acts as a soft buffer to limit the LiPS shuttle effect through chemical absorption and further serves as an auxiliary "current collector" to enhance the electronic conductivity of the sulfur cathode.[242] Yi *et al.* presented a lightweight, dual-functional separator for lithium–sulfur batteries, developed through a physical blend and blade-coating technique using carbon black/poly(3,4-ethylene dioxythiophene) (styrene sulfonate) (CB/PEDOT). This separator significantly enhances sulfur utilization by functioning as a co-current collector and effectively inhibits polysulfide diffusion while promoting lithium ion migration. The modified separator demonstrated an initial capacity of 1315 mA h g^{-1} at 0.2 C, retaining 956 mA h g^{-1} after 100 cycles, and achieved a discharge capacity of 699 mA h g^{-1} at 2 C. With an areal density of just 0.604 mg cm^{-2}, it also offers a specific electrode capacity of 522 mA h g^{-1} at 1 C, showcasing superior performance compared with cells lacking an interlayer (Fig. 25).[243]

3.4 Other applications

In addition to the applications mentioned previously, CPEs exhibit both ionic and conductive properties, showcasing high polarity, excellent crystallinity, and semiconductor characteristics. These materials have found extensive applications in a variety of fields, including optoelectronics, biological applications, sensing, and imaging.[28,244–246] Organic semiconductors, in particular, can be easily modified to enhance their electronic properties. For instance, their band gaps can be finely tuned, and they exhibit a broad absorption range alongside high charge carrier mobility, making them particularly suitable for photocatalytic hydrogen evolution.[247] The principle of photocatalytic hydrogen production involves using a photocatalyst to absorb light energy, which excites electrons and generates electron–hole pairs. Specifically, the process follows these steps: the photocatalyst absorbs photons, causing electrons to transition from the valence band to the conduction band, forming electron–hole pairs. The excited electrons then move to the catalyst surface, where they participate in the reduction of hydrogen ions to produce hydrogen gas. Simultaneously, the holes facilitate the oxidation of water to generate oxygen gas. To enhance the efficiency of this process, the energy band structure of the catalyst must meet the redox potential requirements, and minimizing electron–hole recombination as well as optimizing surface reactions are essential.[248,249] Efficient photocatalytic hydrogen evolution has been achieved by modifying the interaction between CPEs and co-catalysts. Water-soluble CPEs, in particular, have demonstrated significant improvements in photocatalytic performance. Furthermore, the photocatalytic activity of CPEs can be precisely tuned through molecular engineering, such as varying the side chains and counterions in the CPEs, thereby influencing their interaction with Pt co-catalysts.[54] For instance, Hu *et al.* developed a series of novel cationic CPEs to enhance photocatalytic hydrogen production. By incorporating cationic side chains into the polymer backbone, they signifi-

© 2025 The Author(s). Published by the Royal Society of Chemistry

Open Access Article. Published on 14 März 2025. Downloaded on 28.01.2026 01:53:57.
This article is licensed under a Creative Commons Attribution-NonCommercial 3.0 Unported Licence.

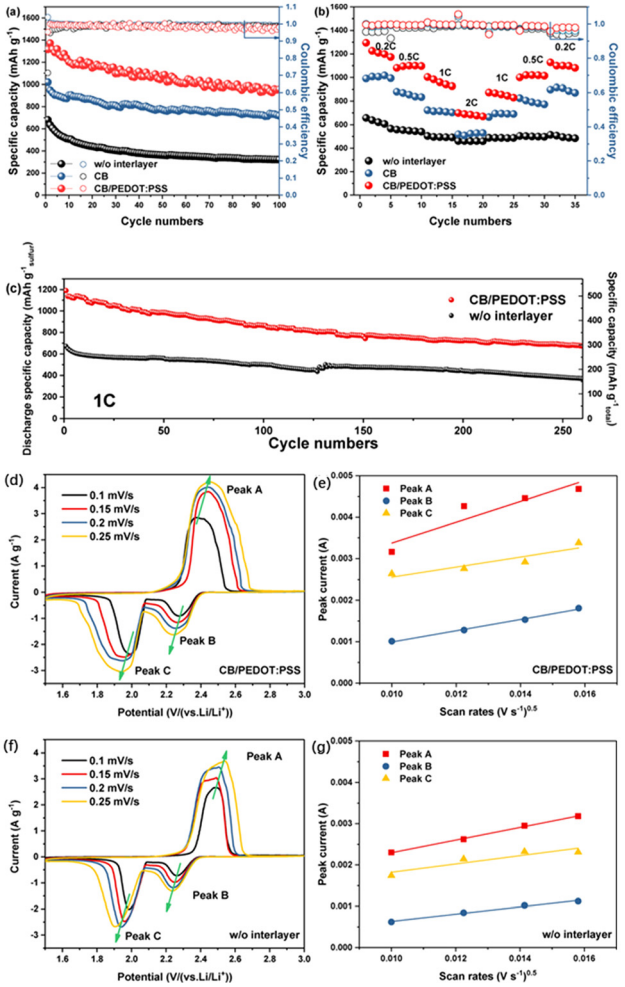

Fig. 25 (a) The cyclic discharging specific capacities and coulombic efficiency of cell without interlayer, with CB or CB/PEDOT:PSS interlayer at 0.2 C current density. (b) The rate capacities of cells with CB or CB/PEDOT:PSS interlayer. (c) Long-term cycling of CB/PEDOT:PSS cell at 1 C. CV curves recorded at different scan rates for Li–S batteries with (d) CB/PEDOT:PSS modified separator and (f) without interlayer. Linear fits of CV peak current dependence based on the scan rate of Li–S batteries with (e) CB/PEDOT:PSS modified separator and (g) without interlayer.[243]

cantly improved both the solubility in polar solvents and the photocatalytic activity. The synthesized CPEs, which incorporated different co-monomers such as BT, DTBT, and DPP, exhibited superior light absorption properties and progressively reduced energy gaps. When combined with PFN-Br, these materials exhibited a hydrogen generation rate 50 times higher than that of PFN alone. This study also explored the influence of different anions on photocatalytic performance, emphasizing the importance of optimizing the interaction between cations and metal catalysts to improve efficiency.[54] Wu *et al.* further enhanced photocatalytic hydrogen generation by introducing fluorine (–F) and cyano (–CN) substituents, achieving a 2.9-fold and 12-fold increase in hydrogen generation, respectively. Additionally, the introduction of quaternary ammonium salt side chains improved the polymer's dispersion in water, facilitated charge transfer, reduced the bandgap, expanded light absorption, and regulated the stacking distance of the polymers, thereby enhancing charge mobility and crystallinity (Fig. 26).[250,251]

In biotechnology, organic semiconductors have emerged as promising materials due to their functional versatility and high biocompatibility. Conjugated polyelectrolytes, with their charged backbones, combine the desirable absorption and photostability of conjugated polymers with excellent water solubility and biocompatibility.[29,252] These properties make them potential candidates for photothermal therapy (PTT) and photodynamic therapy (PDT), as they can absorb near-infrared light and transfer energy to deeper tissue layers.[244,253,254] The mechanisms of PTT and PDT involve the excitation of photosensitizers (PS) under specific wavelengths of light. In PDT, the PS absorbs light, transitioning from the ground state to an excited singlet state, and then undergoes intersystem crossing to a more stable triplet state. In this state, the PS interacts with oxygen to produce reactive oxygen species (ROS), which cause cellular damage. In contrast, PTT directly uses near-infrared light to heat tissues, inducing cell death. The transition between the ground and excited states plays a crucial role in both therapies, affecting their selectivity and efficacy (Fig. 27).[244,253,254] Chen *et al.* investigated the optical and photothermal properties of two newly synthesized conjugated polymers, PPBBT and Dihexyl-PPBBT. These polymers exhibited broad absorption from 250 to 1200 nm and demonstrated band gaps of 0.69 eV and 0.62 eV, respectively, making them suitable for organic photothermal applications. In photothermal tests, PPBBT showed heating rates comparable to those of single-walled carbon nanotubes (SWCNTs) and achieved a photothermal conversion efficiency of up to 94.3%. Furthermore, the water-soluble nanoparticles, NPPPBBT, encapsulating PPBBT, exhibited excellent stability, photothermal properties, and significant phototoxicity in cell experiments. *In vivo* studies indicated that NPPPBBT, combined with near-infrared laser (NIR) irradiation, effectively suppressed tumor growth, while also displaying excellent biocompatibility, thereby highlighting its potential in cancer therapy.[246] Hu *et al.* developed a novel organic semiconductor conjugated

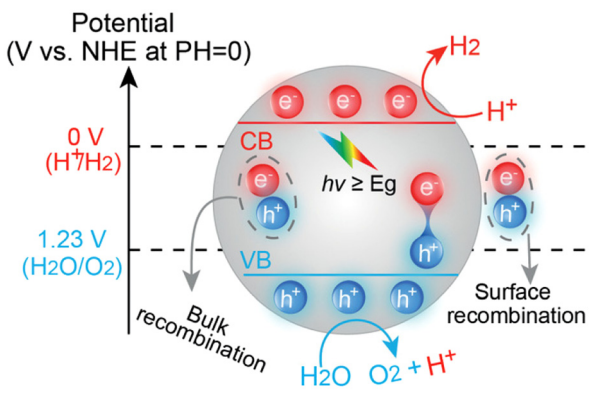

Fig. 26 The schematic process of photocatalytic mechanism.[251]

Open Access Article. Published on 14 März 2025. Downloaded on 28.01.2026 01:53:57.
This article is licensed under a Creative Commons Attribution-NonCommercial 3.0 Unported Licence.

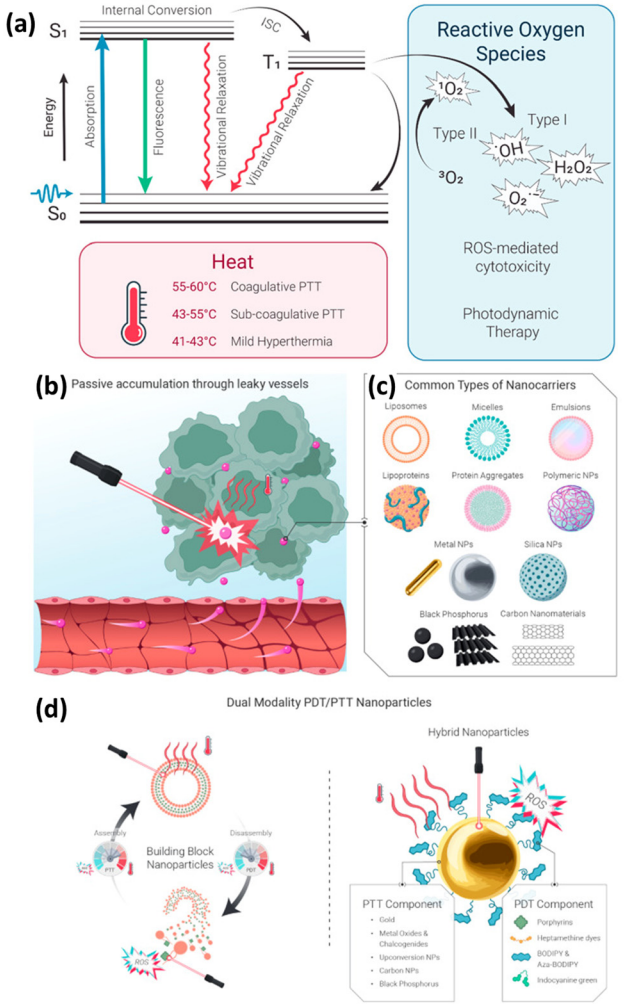

Fig. 27 (a) Simplified Jablonski diagram illustrating the photophysical and photochemical basis of PDT and PTT. S_0 – ground state, S_1 – excited singlet state, T_1 – excited triplet state, ISC – intersystem crossing. Use of nanoparticles for dual PDT/PTT treatment. (b) Nanoparticles passively accumulate in tumors due to the EPR effect, where they can be activated with light to produce ROS or heat. (c) Common delivery vehicles include liposomes, micelles, nanoemulsions, lipoproteins and lipoprotein mimetics, protein-based nanoparticles, polymeric nanoparticles, metal, silica, black-phosphorus and carbon-based nanomaterials. (d) Left panel: PDT/PTT-active nanoparticles can be designed with a single monomer that can act as a PTT agent within an intact nanostructure and a PS upon dissociation. Right panel: hybrid PDT/PTT-active nanoparticles can incorporate two or more photoactive agents, one of which acts as a PS, while another enhances heat generation.[254]

polymer, PCP-SO_3K, as a photothermal agent for NIR photothermal therapy (PTT). *In vitro* experiments showed that PCP-SO_3K exhibited low toxicity to HeLa and 4T1 cells, significantly inhibiting cancer cell growth and inducing apoptosis upon laser irradiation. Further animal studies revealed that PCP-SO_3K, when combined with laser irradiation, effectively suppressed tumor growth in a 4T1 tumor mouse model, achieving complete remission without causing damage to major organs, demonstrating its excellent biocompatibility.[255] Yuan *et al.* introduced a platform for combined chemotherapy and PDT, incorporating inorganic upconversion nanoparticles (UCNP) with CPEs. Targeting the cyclic arginine-glycine-aspartic acid (cRGD) peptide, the system enhanced drug accumulation in cancer cells overexpressing integrin αvβ3, such as U87-MG cells. Experimental results demonstrated that T-UCNP@CPE–DOX exhibited significant uptake and ROS generation in U87-MG cells, with effective DOX release under NIR irradiation. The platform showed excellent biocompatibility and synergistic therapeutic effects, with a combination index (C.I.) of 0.56, making it a promising approach for selective cancer cell killing and controlled drug release.[253]

Bioelectrochemical Systems (BES) employ electroactive microorganisms interfaced with electrodes to sustainably convert organic matter into electricity or chemicals. Key components include modified electrodes (anode for oxidation, cathode for reduction), microbial communities (bacteria, archaea, fungi) catalyzing redox reactions, conductive electrolytes enabling ionic transport, and a separator membrane preventing electrode interference in dual-chamber designs.[256] Some systems utilize microbially produced electron mediators to enhance charge transfer. By optimizing electrode materials, membrane selection, and microbial activity, BES achieve efficient energy conversion and resource recovery, with applications in renewable power generation, wastewater treatment, and chemical synthesis through integrated biological-electrochemical processes (Fig. 28).[257–259]

These components work synergistically to optimize electrochemical reactions in microbial catalysis, directly impacting power density and overall system performance. The efficiency of extracellular electron transfer (EET) is a crucial factor in the performance of bioelectrochemical processes. Despite challenges related to interfacial contact and bacterial loading, strategies such as the use of 3D electrodes and conductive materials have proved effective in enhancing EET efficiency. Recent advancements highlight the potential of CPEs in improving microbial electrosynthesis by promoting more efficient electron transfer to bacteria for substrate reduction.

Bazan *et al.* explored the role played by BES in sustainable energy conversion between electrical and chemical energy. They demonstrated how a single conjugated polymer can enhance bidirectional extracellular electron transfer through self-assembled coatings on microbial cells. Specifically, the n-type conjugated polyelectrolyte, p(cNDI-gT2), facilitates electron transfer involving the outer membrane cytochromes and flavins of *Shewanella oneidensis* MR-1, within a reduction potential range of −0.1 to −0.8 V. Electrochemical tests revealed that electron injection from an external electrode into *Shewanella oneidensis* MR-1 is effective at −0.6 V, while electron extraction occurs at 0.2 V. Compared with control systems, this biohybrid exhibited a sixfold increase in biocurrent generation and a 35-fold increase in current uptake for the electrosynthesis of succinate, demonstrating new strategies for the design of multifunctional biohybrids.[260]

Additionally, they designed and synthesized a new n-type conductive polymer electrolyte (CPE), p(ziNDI-gT2), to serve as the conductive matrix in a 3D living bioelectrochemical composite. Key design elements of this molecule include: (1) an *n*-dopable conjugated polymer backbone with excellent redox stability in

© 2025 The Author(s). Published by the Royal Society of Chemistry

Open Access Article. Published on 14 März 2025. Downloaded on 28.01.2026 01:53:57.
This article is licensed under a Creative Commons Attribution-NonCommercial 3.0 Unported Licence.

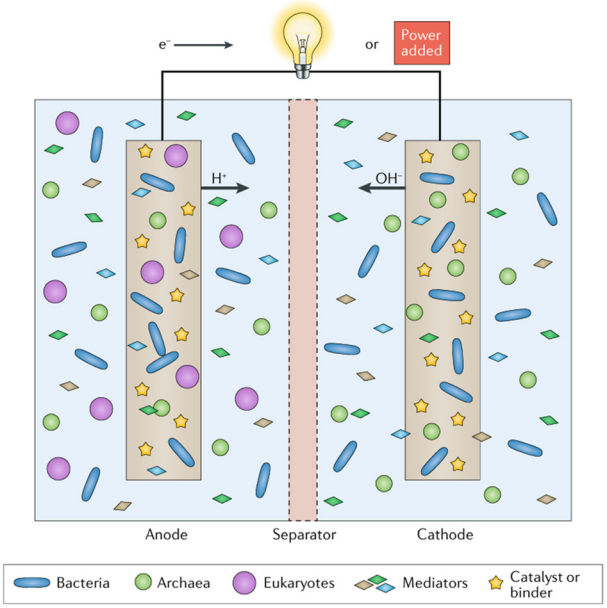

Fig. 28 Components of microbial fuel cells and other bioelectrochemical systems.[256]

water; and (2) zwitterionic side chains that enhance water processability and self-assembly capabilities. Through self-assembly, this biocomposite amplified cellular current uptake by approximately 674-fold compared with *S. oneidensis* MR-1 without the CPE. The enhanced current uptake was attributed to an increase in the number of cells in electronic communication with the electrode, as well as a higher current uptake per cell. This was facilitated by the interconnected porous CPE network, which enabled bacterial interpenetration and facilitated extensive charge distribution throughout the matrix, supporting long-range EET.[261]

In addition to these applications, CPEs have significant potential in the biomedical field due to their tunable luminescence properties and excellent stability. They have been demonstrated as promising fluorescent probes for disease detection, imaging, and therapy.[262] The adjustable luminescence characteristics and remarkable stability of CPEs make them ideal candidates for enhancing detection signals, with widespread use in the sensitive detection of DNA/RNA and intracellular imaging. As derivatives of conjugated polyelectrolytes, membrane-intercalating conjugated oligoelectrolytes (MICOEs) exhibit exceptional capabilities as biomimetic materials.[29] By mimicking the structural properties of lipid bilayers, these molecules can stably integrate with biological cell membranes, facilitating functional modifications.[263,264] Recent advancements by Meng *et al.* have demonstrated the design of novel MICOE molecules that achieve efficient incorporation into liposomes. These molecules enable *in vivo* fluorescence imaging in the second near-infrared window (NIR-II), surpassing traditional carbocyanine dyes in both compatibility and photophysical performance.[265] Their application in liposome tracking provides critical insights into pharmacokinetics and promotes research in drug delivery systems.

4 Outlook

Conjugated polyelectrolytes (CPEs) have garnered significant attention due to their unique combination of high ionic–electronic conductivity, tunable electronic properties, and excellent biocompatibility. These organic semiconductors are reshaping the frontiers of semiconductor technology through their distinctive ion–electron coupling transport characteristics, demonstrating potential to complement or even replace traditional inorganic semiconductors in flexible electronics, bio-interfacial devices, and sustainable energy systems. Nevertheless, their application translation faces multidimensional challenges spanning material performance, mechanistic understanding, and engineering applications.

The primary challenges can be systematically categorized into three dimensions. First, the intrinsic trade-off between electrical conductivity and structural stability fundamentally limits their practical deployment in demanding environments. Additionally, the lack of mechanistic understanding regarding multiscale ion–electron coupling transport mechanisms hinders the rational design of advanced CPE materials. Furthermore, the emerging applications outlined in this review, such as energy storage systems and OECTs, may serve as promising application avenues or not. Particularly, the ionic–electronic coupling characteristics of CPEs could potentially address critical challenges.

To address these challenges, these strategic research directions require urgent attention. Primarily, establishing systematic molecular design strategies and structure-performance relationship is crucial for achieving balanced ionic electronic performance. This involves precisely engineering backbone conjugation length, side-chain ionic density, and counterion mobility through advanced polymerization techniques. Moreover, deciphering the dynamic ion–electron coupling mechanisms demands the integration of multiscale characterization techniques spanning from *in situ* spectroscopic analysis to mesoscale device modeling. Future research should prioritize three breakthrough directions: (1) innovating dynamic doping strategies that enable real-time modulation of ionic–electronic coupling; (2) establishing theoretical frameworks combining density functional theory calculations with coarse-grained molecular dynamics simulations; (3) developing environmentally stable CPE derivatives through molecular encapsulation engineering. The convergence of these approaches will not only deepen our fundamental understanding of CPE systems but also accelerate their translation into practical applications ranging from implantable bioelectronics to large-area energy harvesting devices.

In conclusion, while CPEs present transformative potential across multiple technological domains, realizing their full capabilities requires coordinated efforts in material innovation, mechanistic elucidation, and engineering optimization. Breaking through these scientific and technological bottlenecks will ultimately establish CPEs as a new paradigm in multifunctional semiconductor materials.

© 2025 The Author(s). Published by the Royal Society of Chemistry

Open Access Article. Published on 14 März 2025. Downloaded on 28.01.2026 01:53:57.
This article is licensed under a Creative Commons Attribution-NonCommercial 3.0 Unported Licence.

Data availability

No primary data were used for this review article.

Conflicts of interest

There are no conflicts to declare.

Acknowledgements

The financial support of the Guangzhou Municipal Science and Technology Bureau (2024A04J3513), Guangdong Basic and Applied Basic Research Foundation (2024A1515011732) and National Natural Science Foundation of China (52303229, 52394273) is greatly appreciated.

References

1 H. Tang, Y. Bai, H. Zhao, X. Qin, Z. Hu, C. Zhou, F. Huang and Y. Cao, *Adv. Mater.*, 2024, **36**, 2212236.
2 J. Wang, K. Lin, K. Zhang, X.-F. Jiang, K. Mahmood, L. Ying, F. Huang and Y. Cao, *Adv. Energy Mater.*, 2016, **6**, 1502563.
3 X. Liu, Z. Chen, R. Xu, R. Zhang, Z. Hu, F. Huang and Y. Cao, *Small Methods*, 2018, **2**, 1700407.
4 S. Arora and N. Verma, *RSC Appl. Polym.*, 2024, **2**, 317–355.
5 Y. H. Kwon, K. Minnici, M. M. Huie, K. J. Takeuchi, E. S. Takeuchi, A. C. Marschilok and E. Reichmanis, *Chem. Mater.*, 2016, **28**, 6689–6697.
6 R. Van Noorden, *Nature*, 2014, **507**, 26–28.
7 K. Bicy, A. B. Gueye, D. Rouxel, N. Kalarikkal and S. Thomas, *Surf. Interfaces*, 2022, **31**, 101977.
8 P. Li and Z.-H. Lu, *Small Sci.*, 2021, **1**, 2000015.
9 H. Liu, J. Song, Z. Zhao, S. Zhao, Z. Tian and F. Yan, *Adv. Sci.*, 2024, **11**, 2305347.
10 L. Zou, Y. Qiao and C. M. Li, *Electrochem. Energy Rev.*, 2018, **1**, 567–598.
11 C. Tan, S. Wang, I. Barboza-Ramos and K. S. Schanze, *ACS Appl. Mater. Interfaces*, 2024, **16**, 19887–19892.
12 H. Shirakawa, E. J. Louis, A. G. MacDiarmid, C. K. Chiang and A. J. Heeger, *J. Chem. Soc., Chem. Commun.*, 1977, 578–580, DOI: **10.1039/C39770000578**.
13 C. K. Chiang, C. R. Fincher, Y. W. Park, A. J. Heeger, H. Shirakawa, E. J. Louis, S. C. Gau and A. G. MacDiarmid, *Phys. Rev. Lett.*, 1978, **40**, 1472–1472.
14 A. J. Heeger, *Chem. Soc. Rev.*, 2010, **39**, 2354–2371.
15 T. Qu, G. Nan, Y. Ouyang, B. Bieketuerxun, X. Yan, Y. Qi and Y. Zhang, *Polymers*, 2023, **15**, 4268.
16 H. Dong and W. Hu, *Acc. Chem. Res.*, 2016, **49**, 2435–2443.
17 C. Duan, K. Zhang, C. Zhong, F. Huang and Y. Cao, *Chem. Soc. Rev.*, 2013, **42**, 9071–9104.
18 S. T. M. Tan, A. Gumyusenge, T. J. Quill, G. S. LeCroy, G. E. Bonacchini, I. Denti and A. Salleo, *Adv. Mater.*, 2022, **34**, 2110406.
19 B. D. Paulsen, K. Tybrandt, E. Stavrinidou and J. Rivnay, *Nat. Mater.*, 2020, **19**, 13–26.
20 Z. Ren, Z. Cui, X. Shi, L. Wang, Y. Dou, F. Wang, H. Lin, H. Yan and S. Chen, *Joule*, 2023, **7**, 2894–2904.
21 S. Zhang, R. Wu, C. Mu, Y. Wang, L. Han, Y. Wu and W.-H. Zhu, *ACS Mater. Lett.*, 2022, **4**, 1976–1983.
22 H. Zhao, Y. Dou, S. Chen, H. Tang, Y. Bai, R. Tan, K. Zhang, C. Liu and F. Huang, *Chem. Mater.*, 2023, **35**, 8695–8705.
23 K. Zhang, R. Xu, W. Ge, M. Qi, G. Zhang, Q.-H. Xu, F. Huang, Y. Cao and X. Wang, *Nano Energy*, 2017, **34**, 164–171.
24 G. Zhang, C. Xie, P. You and S. Li, in *Introduction to Organic Electronic Devices*, Springer Nature Singapore, Singapore, 2022, pp. 207–220. DOI: **10.1007/978-981-19-6091-8_7**.
25 E. Zeglio and O. Inganäs, *Adv. Mater.*, 2018, **30**, 1800941.
26 G. Liu, S. Xun, N. Vukmirovic, X. Song, P. Olalde-Velasco, H. Zheng, V. S. Battaglia, L. Wang and W. Yang, *Adv. Mater.*, 2011, **23**, 4679–4683.
27 M. Wu, X. Xiao, N. Vukmirovic, S. Xun, P. K. Das, X. Song, P. Olalde-Velasco, D. Wang, A. Z. Weber, L.-W. Wang, V. S. Battaglia, W. Yang and G. Liu, *J. Am. Chem. Soc.*, 2013, **135**, 12048–12056.
28 H. Jiang, P. Taranekar, J. R. Reynolds and K. S. Schanze, *Angew. Chem., Int. Ed.*, 2009, **48**, 4300–4316.
29 C. Zhou, G. W. N. Chia and K.-T. Yong, *Chem. Soc. Rev.*, 2022, **51**, 9917–9932.
30 T. J. Quill, G. LeCroy, A. Melianas, D. Rawlings, Q. Thiburce, R. Sheelamanthula, C. Cheng, Y. Tuchman, S. T. Keene, I. McCulloch, R. A. Segalman, M. L. Chabinyc and A. Salleo, *Adv. Funct. Mater.*, 2021, **31**, 2104301.
31 Y. Wang, S. Wustoni, J. Surgailis, Y. Zhong, A. Koklu and S. Inal, *Nat. Rev. Mater.*, 2024, **9**, 249–265.
32 S. T. Keene, A. Rao and G. G. Malliaras, *Sci. Adv.*, 2023, **9**, eadi3536.
33 Y. Tsarfati, K. C. Bustillo, B. H. Savitzky, L. Balhorn, T. J. Quill, A. Marks, J. Donohue, S. E. Zeltmann, C. J. Takacs, A. Giovannitti, I. McCulloch, C. Ophus, A. M. Minor and A. Salleo, *Nat. Mater.*, 2024, **24**, 101–108.
34 C. Zuo, H. J. Bolink, H. Han, J. Huang, D. Cahen and L. Ding, *Adv. Sci.*, 2016, **3**, 1500324.
35 Y. Yao, H. Dong and W. Hu, *Adv. Mater.*, 2016, **28**, 4513–4523.
36 H.-Y. Huang, D. Fan, D. Wang, T. Han and B. Z. Tang, *Polym. Chem.*, 2025, **16**, 923–935.
37 G. Liu, J. Jia, K. Zhang, X. E. Jia, Q. Yin, W. Zhong, L. Li, F. Huang and Y. Cao, *Adv. Energy Mater.*, 2019, **9**, 1803657.
38 Y. Jin, Z. Chen, S. Dong, N. Zheng, L. Ying, X.-F. Jiang, F. Liu, F. Huang and Y. Cao, *Adv. Mater.*, 2016, **28**, 9811–9818.
39 Y. Kim, E. H. Jung, G. Kim, D. Kim, B. J. Kim and J. Seo, *Adv. Energy Mater.*, 2018, **8**, 1801668.
40 Z. Du, Q. Xue, K. Zhang, Z. Hu, Z. Zhou, J. Jing, L. Shao, N. Li and F. Huang, *Sol. RRL*, 2022, **6**, 2200527.
41 S.-H. Jin, W. Ko, S. Lee and Y.-J. Hwang, *Polym. Chem.*, 2022, **13**, 3171–3178.

© 2025 The Author(s). Published by the Royal Society of Chemistry

Open Access Article. Published on 14 März 2025. Downloaded on 28.01.2026 01:53:57.
This article is licensed under a Creative Commons Attribution-NonCommercial 3.0 Unported Licence.

42 Z. Hu, R. Xu, S. Dong, K. Lin, J. Liu, F. Huang and Y. Cao, *Mater. Horiz.*, 2017, **4**, 88–97.
43 C. Liu, K. Wang, X. Gong and A. J. Heeger, *Chem. Soc. Rev.*, 2016, **45**, 4825–4846.
44 Y. Tang, H. Feng, Y. Liang, H. Tang, Z. Du, J. Xu, F. Huang and Y. Cao, *ACS Appl. Polym. Mater.*, 2023, **5**, 2298–2306.
45 G. Zhang, X.-K. Chen, J. Xiao, P. C. Y. Chow, M. Ren, G. Kupgan, X. Jiao, C. C. S. Chan, X. Du, R. Xia, Z. Chen, J. Yuan, Y. Zhang, S. Zhang, Y. Liu, Y. Zou, H. Yan, K. S. Wong, V. Coropceanu, N. Li, C. J. Brabec, J.-L. Bredas, H.-L. Yip and Y. Cao, *Nat. Commun.*, 2020, **11**, 3943.
46 S. Ma, S. Wu, J. Zhang, Y. Song, H. Tang, K. Zhang, F. Huang and Y. Cao, *ACS Appl. Mater. Interfaces*, 2020, **12**, 51776–51784.
47 P. Liu, K. Zhang, F. Liu, Y. Jin, S. Liu, T. P. Russell, H.-L. Yip, F. Huang and Y. Cao, *Chem. Mater.*, 2014, **26**, 3009–3017.
48 G. Liu, T. Jia, K. Zhang, J. Jia, Q. Yin, W. Zhong, X. E. Jia, N. Zheng, L. Ying, F. Huang and Y. Cao, *Chem. Mater.*, 2020, **32**, 1022–1030.
49 S. Ma, Q. Huang, Y. Liang, H. Tang, Y. Chen, J. Zhang, K. Zhang, F. Huang and Y. Cao, *J. Mater. Chem. C*, 2021, **9**, 13896–13903.
50 Y. Li, D. Zhang, Z. Huang, T. Zhang, N. Zheng, F. Peng, L. Ying and F. Huang, *J. Mater. Chem. C*, 2023, **11**, 15426–15434.
51 L. Li, G. Liu, J. Zhang, Z. Wang, T. Jia, Y. Hu, C. Cao, K. Zhang, F. Huang and Y. Cao, *J. Mater. Chem. C*, 2019, **7**, 4709–4715.
52 W. Zhong, J. Cui, B. Fan, L. Ying, Y. Wang, X. Wang, G. Zhang, X.-F. Jiang, F. Huang and Y. Cao, *Chem. Mater.*, 2017, **29**, 8177–8186.
53 J. Jiang, Z. Xu, J. Zhou, M. Hanif, Q. Jiang, D. Hu, R. Zhao, C. Wang, L. Liu, D. Ma, Y. Ma and Y. Cao, *Chem. Mater.*, 2019, **31**, 6499–6505.
54 Z. Hu, X. Zhang, Q. Yin, X. Liu, X. Jiang, Z. Chen, X. Yang, F. Huang and Y. Cao, *Nano Energy*, 2019, **60**, 775–783.
55 C. Zhou, Z. Chen, G. Zhang, C. McDowell, P. Luo, X. Jia, M. J. Ford, M. Wang, G. C. Bazan, F. Huang and Y. Cao, *Adv. Energy Mater.*, 2018, **8**, 1701668.
56 C. Zhou, Y. Liang, F. Liu, C. Sun, X. Huang, Z. Xie, F. Huang, J. Roncali, T. P. Russell and Y. Cao, *Adv. Funct. Mater.*, 2014, **24**, 7538–7547.
57 J. Jiang, D. Hu, M. Hanif, X. Li, S. Su, Z. Xie, L. Liu, S. Zhang, B. Yang and Y. Ma, *Adv. Opt. Mater.*, 2016, **4**, 2109–2118.
58 L. Shao, L. Hong, Y. Cao, H. Tang, Y. Huang, X. Xia, Y. Bai, M. Dong, X. Zhang, X. Lu, X. Yang, C. Liu, F. Huang and Y. Cao, *Adv. Opt. Mater.*, 2023, **11**, 2202823.
59 Y. Wang, L. Sun, C. Wang, F. Yang, X. Ren, X. Zhang, H. Dong and W. Hu, *Chem. Soc. Rev.*, 2019, **48**, 1492–1530.
60 I. McCulloch, M. Heeney, C. Bailey, K. Genevicius, I. MacDonald, M. Shkunov, D. Sparrowe, S. Tierney, R. Wagner, W. Zhang, M. L. Chabinyc, R. J. Kline, M. D. McGehee and M. F. Toney, *Nat. Mater.*, 2006, **5**, 328–333.
61 T. Lei, J.-H. Dou and J. Pei, *Adv. Mater.*, 2012, **24**, 6457–6461.
62 K. Zhang, Z. Chen, A. Armin, S. Dong, R. Xia, H.-L. Yip, S. Shoaee, F. Huang and Y. Cao, *Sol. RRL*, 2018, **2**, 1700169.
63 B. Meng, J. Liu and L. Wang, *Polym. Chem.*, 2020, **11**, 1261–1270.
64 Z. Zhong, S. Chen, J. Zhao, J. Xie, K. Zhang, T. Jia, C. Zhu, J. Jing, Y. Liang, L. Hong, S. Zhu, D. Ma and F. Huang, *Adv. Energy Mater.*, 2023, **13**, 2302273.
65 Y. Zheng, S. Zhang, J. B. H. Tok and Z. Bao, *J. Am. Chem. Soc.*, 2022, **144**, 4699–4715.
66 K. Zhang, C. Zhong, S. Liu, A.-H. Liang, S. Dong and F. Huang, *J. Mater. Chem. C*, 2014, **2**, 3270–3277.
67 J. Tang, C. Liao, Y. Duan, X. Xu, M. Deng, L. Yu, R. Li and Q. Peng, *Angew. Chem., Int. Ed.*, 2022, **61**, e202213252.
68 Z. Wang, Z. Liu, L. Ning, M. Xiao, Y. Yi, Z. Cai, A. Sadhanala, G. Zhang, W. Chen, H. Sirringhaus and D. Zhang, *Chem. Mater.*, 2018, **30**, 3090–3100.
69 S. Pang, B. Wu, B. Zhang, R. Zhang, C. Reckmeier, E. Zhou, C. Duan, F. Huang and Y. Cao, *J. Mater. Chem. C*, 2021, **9**, 9515–9523.
70 K. Zhang, B. Fan, R. Xia, X. Liu, Z. Hu, H. Gu, S. Liu, H.-L. Yip, L. Ying, F. Huang and Y. Cao, *Adv. Energy Mater.*, 2018, **8**, 1703180.
71 E. H. Jung, N. J. Jeon, E. Y. Park, C. S. Moon, T. J. Shin, T.-Y. Yang, J. H. Noh and J. Seo, *Nature*, 2019, **567**, 511–515.
72 S. Holliday, R. S. Ashraf, A. Wadsworth, D. Baran, S. A. Yousaf, C. B. Nielsen, C.-H. Tan, S. D. Dimitrov, Z. Shang, N. Gasparini, M. Alamoudi, F. Laquai, C. J. Brabec, A. Salleo, J. R. Durrant and I. McCulloch, *Nat. Commun.*, 2016, **7**, 11585.
73 P. Xu, L. Zheng, W. Feng, L. Yang, P. Song, J. Luo, W. Tian, W. Gao, C. Tian, L. Xie, E. L. Lim and Z. Wei, *Mater. Today Energy*, 2024, **41**, 101523.
74 A. Wadsworth, Z. Hamid, M. Bidwell, R. S. Ashraf, J. I. Khan, D. H. Anjum, C. Cendra, J. Yan, E. Rezasoltani, A. A. Y. Guilbert, M. Azzouzi, N. Gasparini, J. H. Bannock, D. Baran, H. Wu, J. C. de Mello, C. J. Brabec, A. Salleo, J. Nelson, F. Laquai and I. McCulloch, *Adv. Energy Mater.*, 2018, **8**, 1801001.
75 Q. Hu, E. Rezaee, M. Li, Q. Chen, C. Li, S. Cai, H. Shan and Z.-X. Xu, *Sol. RRL*, 2020, **4**, 1900340.
76 H. Yano, K. Kudo, K. Marumo and H. Okuzaki, *Sci. Adv.*, 2019, **5**, eaav9492.
77 R. Yang, A. Garcia, D. Korystov, A. Mikhailovsky, G. C. Bazan and T.-Q. Nguyen, *J. Am. Chem. Soc.*, 2006, **128**, 16532–16539.
78 Y. Liang, H. Tang, C. Zhang, C. Liu, L. Lan and F. Huang, *ACS Appl. Mater. Interfaces*, 2022, **14**, 51165–51174.
79 D. Izuhara and T. M. Swager, *J. Am. Chem. Soc.*, 2009, **131**, 17724–17725.
80 S. Rochat and T. M. Swager, *J. Am. Chem. Soc.*, 2013, **135**, 17703–17706.
81 D. Izuhara and T. M. Swager, *J. Mater. Chem.*, 2011, **21**, 3579–3584.

© 2025 The Author(s). Published by the Royal Society of Chemistry

Open Access Article. Published on 14 März 2025. Downloaded on 28.01.2026 01:53:57.
This article is licensed under a Creative Commons Attribution-NonCommercial 3.0 Unported Licence.

82 P. Li, W. Sun, J. Li, J.-P. Chen, X. Wang, Z. Mei, G. Jin, Y. Lei, R. Xin, M. Yang, J. Xu, X. Pan, C. Song, X.-Y. Deng, X. Lei, K. Liu, X. Wang, Y. Zheng, J. Zhu, S. Lv, Z. Zhang, X. Dai and T. Lei, *Science*, 2024, **384**, 557–563.
83 T. M. Pappenfus, F. Almyahi, N. A. Cooling, E. W. Culver, S. C. Rasmussen and P. C. Dastoor, *Macromol. Chem. Phys.*, 2018, **219**, 1800272.
84 J.-R. Pouliot, F. Grenier, J. T. Blaskovits, S. Beaupré and M. Leclerc, *Chem. Rev.*, 2016, **116**, 14225–14274.
85 A. Facchetti, L. Vaccaro and A. Marrocchi, *Angew. Chem., Int. Ed.*, 2012, **51**, 3520–3523.
86 A. Marrocchi, D. Lanari, A. Facchetti and L. Vaccaro, *Energy Environ. Sci.*, 2012, **5**, 8457–8474.
87 Y. Liu, K. Xian, R. Gui, K. Zhou, J. Liu, M. Gao, W. Zhao, X. Jiao, Y. Deng, H. Yin, Y. Geng and L. Ye, *Macromolecules*, 2022, **55**, 133–145.
88 C. Zhai, X. Yang, S. Han, G. Lu, P. Wei, A. Chumakov, E. Erbes, Q. Chen, S. Techert, S. V. Roth, P. Zhang and L. Bu, *Chem. Mater.*, 2021, **33**, 2673–2682.
89 Y. Na and F. S. Kim, *Chem. Mater.*, 2019, **31**, 4759–4768.
90 G. Barbarella, M. Zangoli and F. Di Maria, in *Adv. Heterocycl. Chem*, ed. E. F. V. Scriven and C. A. Ramsden, Academic Press, 2017, vol. 123, pp. 105–167.
91 L. V. Kayser and D. J. Lipomi, *Adv. Mater.*, 2019, **31**, 1806133.
92 L. Groenendaal, F. Jonas, D. Freitag, H. Pielartzik and J. R. Reynolds, *Adv. Mater.*, 2000, **12**, 481–494.
93 B. Zhao, S. Chung, M. Zhang, W. Wei, C. Zhu, C. Deng, K. Cho and Z. Kan, *Adv. Funct. Mater.*, 2024, **34**, 2309832.
94 J. Jing, S. Dong, K. Zhang, Z. Zhou, Q. Xue, Y. Song, Z. Du, M. Ren and F. Huang, *Adv. Energy Mater.*, 2022, **12**, 2200453.
95 Y. Jin, Z. Chen, M. Xiao, J. Peng, B. Fan, L. Ying, G. Zhang, X.-F. Jiang, Q. Yin, Z. Liang, F. Huang and Y. Cao, *Adv. Energy Mater.*, 2017, **7**, 1700944.
96 J. Zhang, C.-H. Tan, K. Zhang, T. Jia, Y. Cui, W. Deng, X. Liao, H. Wu, Q. Xu, F. Huang and Y. Cao, *Adv. Energy Mater.*, 2021, **11**, 2102559.
97 Y. Song, K. Zhang, S. Dong, R. Xia, F. Huang and Y. Cao, *ACS Appl. Mater. Interfaces*, 2020, **12**, 18473–18481.
98 Z. Hu, F. Huang and Y. Cao, *Small Methods*, 2017, **1**, 1700264.
99 H. S. Kang, D. H. Kim and T. W. Kim, *Sci. Rep.*, 2021, **11**, 3885.
100 R. Su, S. H. Park, X. Ouyang, S. I. Ahn and M. C. McAlpine, *Sci. Adv.*, 2022, **8**, eabl8798.
101 H. Xu, X. Zhao, G. Yang, X. Ji, X. Zhang, L. Li, B. Wu, X. Ouyang, Y. Ni, L. Chen and H.-C. Hu, *Chem. Eng. J.*, 2022, **430**, 133014.
102 Y. Tian, T. Wang, Q. Zhu, X. Zhang, A. S. Ethiraj, W.-M. Geng and H.-Z. Geng, *Nanomaterials*, 2021, **11**, 2067.
103 X. Karagiorgis, D. Shakthivel, G. Khandelwal, R. Ginesi, P. J. Skabara and R. Dahiya, *ACS Appl. Mater. Interfaces*, 2024, **16**, 19551–19562.
104 G. Li, K. Huang, J. Deng, M. Guo, M. Cai, Y. Zhang and C. F. Guo, *Adv. Mater.*, 2022, **34**, 2200261.
105 X. Fan, W. Nie, H. Tsai, N. Wang, H. Huang, Y. Cheng, R. Wen, L. Ma, F. Yan and Y. Xia, *Adv. Sci.*, 2019, **6**, 1900813.
106 Y. Liang, A. Offenhäusser, S. Ingebrandt and D. Mayer, *Adv. Healthcare Mater.*, 2021, **10**, 2100061.
107 X. Wang, A. K. K. Kyaw, C. Yin, F. Wang, Q. Zhu, T. Tang, P. I. Yee and J. Xu, *RSC Adv.*, 2018, **8**, 18334–18340.
108 H. Tang, Z. Liu, Z. Hu, Y. Liang, F. Huang and Y. Cao, *Sci. China: Chem.*, 2020, **63**, 802–809.
109 S. Inal, G. G. Malliaras and J. Rivnay, *Nat. Commun.*, 2017, **8**, 1767.
110 C. J. Neef and J. P. Ferraris, *Macromolecules*, 2000, **33**, 2311–2314.
111 J. Q. M. Almarashi, A. S. Gadallah, M. A. Ellabban and A.-A. H. Mohamed, *Opt. Mater.*, 2024, **150**, 115240.
112 H. L. Wang, A. G. MacDiarmid, Y. Z. Wang, D. D. Gebier and A. J. Epstein, *Synth. Met.*, 1996, **78**, 33–37.
113 B. E. Conway, V. Birss and J. Wojtowicz, *J. Power Sources*, 1997, **66**, 1–14.
114 M.-Y. Chang, C.-S. Wu, Y.-F. Chen, B.-Z. Hsieh, W.-Y. Huang, K.-S. Ho, T.-H. Hsieh and Y.-K. Han, *Org. Electron.*, 2008, **9**, 1136–1139.
115 J.-C. Chiang and A. G. MacDiarmid, *Synth. Met.*, 1986, **13**, 193–205.
116 Y. Cao, P. Smith and A. J. Heeger, *Synth. Met.*, 1992, **48**, 91–97.
117 F. Huang, H. Wu, D. Wang, W. Yang and Y. Cao, *Chem. Mater.*, 2004, **16**, 708–716.
118 W. Xue, J.-Y. Lin, B. Liu, N.-E. Shi, M.-N. Yu, W.-D. Wu, W.-S. Zhu, L.-H. Xie, L.-H. Wang and W. Huang, *Polymer*, 2018, **153**, 338–343.
119 H. Tang, Z. Liu, Y. Tang, Z. Du, Y. Liang, Z. Hu, K. Zhang, F. Huang and Y. Cao, *Giant*, 2021, **6**, 100053.
120 Q. Kang, L. Ye, B. Xu, C. An, S. J. Stuard, S. Zhang, H. Yao, H. Ade and J. Hou, *Joule*, 2019, **3**, 227–239.
121 S. Wang, J. Li, X. Liu, Q. Zhang, X. Yu and Y. Han, *Polym. Chem.*, 2024, **15**, 4107–4114.
122 Z. Hu, Z. Chen, J. Jing, Y. Liang, Y. Bai, X. Liu, F. Huang and Y. Cao, *J. Mater. Chem. C*, 2020, **8**, 15158–15167.
123 Z.-G. Zhang, B. Qi, Z. Jin, D. Chi, Z. Qi, Y. Li and J. Wang, *Energy Environ. Sci.*, 2014, **7**, 1966–1973.
124 Z. Wu, C. Sun, S. Dong, X.-F. Jiang, S. Wu, H. Wu, H.-L. Yip, F. Huang and Y. Cao, *J. Am. Chem. Soc.*, 2016, **138**, 2004–2013.
125 C.-K. Mai, H. Zhou, Y. Zhang, Z. B. Henson, T.-Q. Nguyen, A. J. Heeger and G. C. Bazan, *Angew. Chem., Int. Ed.*, 2013, **52**, 12874–12878.
126 Y. Zhang, J. Song, J. Qu, P.-C. Qian and W.-Y. Wong, *Sci. China: Chem.*, 2021, **64**, 341–357.
127 W. W. Bao, R. Li, Z. C. Dai, J. Tang, X. Shi, J. T. Geng, Z. F. Deng and J. Hua, *Front. Chem.*, 2020, **8**, 679.
128 J. Humphreys, F. Malagreca, P. A. Hume, E. S. Davies, S. P. Argent, T. D. Bradshaw and D. B. Amabilino, *Chem. Commun.*, 2023, **59**, 1613–1616.
129 M. Zhu, Y. Guo and Y. Liu, *Sci. China: Chem.*, 2022, **65**, 1225–1264.

© 2025 The Author(s). Published by the Royal Society of Chemistry

Open Access Article. Published on 14 März 2025. Downloaded on 28.01.2026 01:53:57.
This article is licensed under a Creative Commons Attribution-NonCommercial 3.0 Unported Licence.

130 J.-L. Li, Y.-F. Chai, W. V. Wang, Z.-F. Shi, Z.-G. Xu and H.-L. Zhang, *Chem. Commun.*, 2017, **53**, 5882–5885.
131 L. Ding, Z.-Y. Wang, J.-Y. Wang and J. Pei, *Chin. J. Chem.*, 2020, **38**, 13–24.
132 H. Sun, X. Guo and A. Facchetti, *Chem*, 2020, **6**, 1310–1326.
133 K. Shi, F. Zhang, C.-A. Di, T.-W. Yan, Y. Zou, X. Zhou, D. Zhu, J.-Y. Wang and J. Pei, *J. Am. Chem. Soc.*, 2015, **137**, 6979–6982.
134 H. Tang, Y. Liang, C. Liu, Z. Hu, Y. Deng, H. Guo, Z. Yu, A. Song, H. Zhao, D. Zhao, Y. Zhang, X. Guo, J. Pei, Y. Ma, Y. Cao and F. Huang, *Nature*, 2022, **611**, 271–277.
135 C. W. Tang, *Appl. Phys. Lett.*, 1986, **48**, 183–185.
136 G. Yu, J. Gao, J. C. Hummelen, F. Wudl and A. J. Heeger, *Science*, 1995, **270**, 1789–1791.
137 Y. Tong, Z. Xiao, X. Du, C. Zuo, Y. Li, M. Lv, Y. Yuan, C. Yi, F. Hao, Y. Hua, T. Lei, Q. Lin, K. Sun, D. Zhao, C. Duan, X. Shao, W. Li, H.-L. Yip, Z. Xiao, B. Zhang, Q. Bian, Y. Cheng, S. Liu, M. Cheng, Z. Jin, S. Yang and L. Ding, *Sci. China: Chem.*, 2020, **63**, 758–765.
138 V. D. Mitchell and D. J. Jones, *Polym. Chem.*, 2018, **9**, 795–814.
139 Y. Dou, L. Hong, J. Jing, T. Jia, J. Zhang, K. Zhang and F. Huang, *Sol. RRL*, 2023, **7**, 2300599.
140 C. Zhou, G. Zhang, C. Zhong, X. Jia, P. Luo, R. Xu, K. Gao, X. Jiang, F. Liu, T. P. Russell, F. Huang and Y. Cao, *Adv. Energy Mater.*, 2017, **7**, 1601081.
141 M. Liu, Y. Gao, Y. Zhang, Z. Liu and L. Zhao, *Polym. Chem.*, 2017, **8**, 4613–4636.
142 J.-P. Correa-Baena, M. Saliba, T. Buonassisi, M. Grätzel, A. Abate, W. Tress and A. Hagfeldt, *Science*, 2017, **358**, 739–744.
143 Q. Jiang and K. Zhu, *Nat. Rev. Mater.*, 2024, **9**, 399–419.
144 S. Dong, Z. Hu, K. Zhang, Q. Yin, X. Jiang, F. Huang and Y. Cao, *Adv. Mater.*, 2017, **29**, 1701507.
145 H.-S. Kim, J.-Y. Seo and N.-G. Park, *ChemSusChem*, 2016, **9**, 2528–2540.
146 L. Tian, Z. Hu, X. Liu, Z. Liu, P. Guo, B. Xu, Q. Xue, H.-L. Yip, F. Huang and Y. Cao, *ACS Appl. Mater. Interfaces*, 2019, **11**, 5289–5297.
147 Y. Yang and J. You, *Nature*, 2017, **544**, 155–156.
148 A. Fakharuddin, L. Schmidt-Mende, G. Garcia-Belmonte, R. Jose and I. Mora-Sero, *Adv. Energy Mater.*, 2017, **7**, 1700623.
149 Y. Li, Y. Wang, Z. Xu, B. Peng and X. Li, *ACS Nano*, 2024, **18**, 10688–10725.
150 X. Yu, Q. Zhou, T. Zheng, R. Peng, B. Fan, L. Fan and B. Jin, *Chem. Eng. J.*, 2023, **452**, 139412.
151 T. Liu, K. Chen, Q. Hu, R. Zhu and Q. Gong, *Adv. Energy Mater.*, 2016, **6**, 1600457.
152 W. Xiang, S. Liu and W. Tress, *Angew. Chem., Int. Ed.*, 2021, **60**, 26440–26453.
153 S. Palei, G. Murali, C.-H. Kim, I. In, S.-Y. Lee and S.-J. Park, *Nano-Micro Lett.*, 2023, **15**, 123.
154 C. M. Wolff, P. Caprioglio, M. Stolterfoht and D. Neher, *Adv. Mater.*, 2019, **31**, 1902762.
155 J. Jing, S. Dong, K. Zhang, B. Xie, J. Zhang, Y. Song and F. Huang, *Nano Energy*, 2022, **93**, 106814.
156 C. Anrango-Camacho, K. Pavón-Ipiales, B. A. Frontana-Uribe and A. Palma-Cando, *Nanomaterials*, 2022, **12**, 443.
157 J. Zhu, Y. Xu, Y. Luo, J. Luo, R. He, C. Wang, Y. Wang, K. Wei, Z. Yi, Z. Gao, J. Wang, J. You, Z. Zhang, H. Lai, S. Ren, X. Liu, C. Xiao, C. Chen, J. Zhang, F. Fu and D. Zhao, *Sci. Adv.*, 2024, **10**, eadl2063.
158 Y. Sun, L. Wang, C. Guo, J. Xiao, C. Liu, C. Chen, W. Xia, Z. Gan, J. Cheng, J. Zhou, Z. Chen, J. Zhou, D. Liu, T. Wang and W. Li, *J. Am. Chem. Soc.*, 2024, **146**, 12011–12019.
159 Y. Bai, Z. Zhou, Q. Xue, C. Liu, N. Li, H. Tang, J. Zhang, X. Xia, J. Zhang, X. Lu, C. J. Brabec and F. Huang, *Adv. Mater.*, 2022, **34**, 2110587.
160 H. Zhou, Y. Zhang, C.-K. Mai, S. D. Collins, T.-Q. Nguyen, G. C. Bazan and A. J. Heeger, *Adv. Mater.*, 2014, **26**, 780–785.
161 S. Moon, S. Khadtare, M. Wong, S.-H. Han, G. C. Bazan and H. Choi, *J. Colloid Interface Sci.*, 2018, **518**, 21–26.
162 Y. Lin, Y. Firdaus, F. H. Isikgor, M. I. Nugraha, E. Yengel, G. T. Harrison, R. Hallani, A. El-Labban, H. Faber, C. Ma, X. Zheng, A. Subbiah, C. T. Howells, O. M. Bakr, I. McCulloch, S. D. Wolf, L. Tsetseris and T. D. Anthopoulos, *ACS Energy Lett.*, 2020, **5**, 2935–2944.
163 Y. Xiao, X. Yang, R. Zhu and H. J. Snaith, *Science*, 2024, **384**, 846–848.
164 Z. Chen, S. Zhang, T. Zhang, J. Dai, Y. Yu, H. Li, X. Hao and J. Hou, *Joule*, 2024, **8**, 1723–1734.
165 C. Li, Z. Zhang, H. Zhang, W. Yan, Y. Li, L. Liang, W. Yu, X. Yu, Y. Wang, Y. Yang, M. K. Nazeeruddin and P. Gao, *Angew. Chem., Int. Ed.*, 2024, **63**, e202315281.
166 M. Liu, L. Bi, W. Jiang, Z. Zeng, S.-W. Tsang, F. R. Lin and A. K.-Y. Jen, *Adv. Mater.*, 2023, **35**, 2304415.
167 R. Liu, J. Xu, T. Hu, X. Li, K. Wang, Q. Huang, Z. Duan, H. Liu, W. Qian, H. Zhou, C. Cong, X. Yue, H. Zhang and F. Xie, *Chem. Eng. J.*, 2025, **505**, 159390.
168 F. Yuan, T. Xue, M. Du, H. Huang, R. Zeng, L. Li, C. Wang, Z. Song, Q. Guo, X. Hu and E. Zhou, *Adv. Funct. Mater.*, 2025, 2425145.
169 H. Tang, Z. Shen, Y. Shen, G. Yan, Y. Wang, Q. Han and L. Han, *Science*, 2024, **383**, 1236–1240.
170 W. Liu, Y. Zang, Y. Tu, Y. Wang, Z. Zhu, C. Zhu and W. Yan, *Small*, 2025, **21**, 2408314.
171 K. Lin, J. Wang, Z. Hu, R. Xu, J. Liu, X. Liu, B. Xu, F. Huang and Y. Cao, *Sol. Energy Mater. Sol. Cells*, 2017, **168**, 22–29.
172 Z. He, C. Zhong, S. Su, M. Xu, H. Wu and Y. Cao, *Nat. Photonics*, 2012, **6**, 591–595.
173 F. Huang, L. Hou, H. Wu, X. Wang, H. Shen, W. Cao, W. Yang and Y. Cao, *J. Am. Chem. Soc.*, 2004, **126**, 9845–9853.
174 J. Luo, H. Wu, C. He, A. Li, W. Yang and Y. Cao, *Appl. Phys. Lett.*, 2009, **95**, 043301.
175 K. Zhang, L. Ying, H.-L. Yip, F. Huang and Y. Cao, *ACS Appl. Mater. Interfaces*, 2020, **12**, 39937–39947.

© 2025 The Author(s). Published by the Royal Society of Chemistry

Open Access Article. Published on 14 März 2025. Downloaded on 28.01.2026 01:53:57.
This article is licensed under a Creative Commons Attribution-NonCommercial 3.0 Unported Licence.

176 K. Zhang, K. Gao, R. Xia, Z. Wu, C. Sun, J. Cao, L. Qian, W. Li, S. Liu, F. Huang, X. Peng, L. Ding, H.-L. Yip and Y. Cao, *Adv. Mater.*, 2016, **28**, 4817–4823.
177 C. Sun, Z. Wu, H.-L. Yip, H. Zhang, X.-F. Jiang, Q. Xue, Z. Hu, Z. Hu, Y. Shen, M. Wang, F. Huang and Y. Cao, *Adv. Energy Mater.*, 2016, **6**, 1501534.
178 L. Feng, S. Chen, K. Zhang, J. Jing, Z. Zhou, Q. Xue, Z. Liu, Y. Chen, S. Dong, F. Huang and Y. Cao, *ACS Appl. Mater. Interfaces*, 2023, **15**, 5566–5576.
179 N. Zheng, Z. Wang, K. Zhang, Y. Li, F. Huang and Y. Cao, *J. Mater. Chem. A*, 2019, **7**, 1429–1434.
180 S. Liu, G. Zhang, J. Lu, J. Jia, W. Li, F. Huang and Y. Cao, *J. Mater. Chem. C*, 2015, **3**, 4372–4379.
181 J. Jia, B. Fan, M. Xiao, T. Jia, Y. Jin, Y. Li, F. Huang and Y. Cao, *Macromolecules*, 2018, **51**, 2195–2202.
182 L. Tian, J. Jing, H. Tang, Y. Liang, Z. Hu, M. Rafiq, F. Huang and Y. Cao, *Sol. RRL*, 2021, **5**, 2000523.
183 M. Rafiq, J. Jing, Y. Liang, Z. Hu, X. Zhang, H. Tang, L. Tian, Y. Li and F. Huang, *Polym. Chem.*, 2021, **12**, 1498–1506.
184 H. Jiang, Q. Liang, H. Guo, A. Zhang, X. Wang, Z. Tang and Z. Bo, *J. Am. Chem. Soc.*, 2024, **146**, 30262–30271.
185 Y. Yu, J. Wang, Z. Chen, Y. Xiao, Z. Fu, T. Zhang, H. Yuan, X.-T. Hao, L. Ye, Y. Cui and J. Hou, *Sci. China: Chem.*, 2024, **67**, 4194–4201.
186 S. Li, X. Zhang, B. Chen, Z. Shi, S. Wu, C. Wang, Q. Tong, M. Zhu and J. Weng, *Electrochim. Acta*, 2024, **483**, 144037.
187 X. Yuan, Y. Zhao, Y. Zhang, D. Xie, W. Deng, J. Li, H. Wu, C. Duan, F. Huang and Y. Cao, *Adv. Funct. Mater.*, 2022, **32**, 2201142.
188 H. Liu, L. Huang, X. Cheng, A. Hu, H. Xu, L. Chen and Y. Chen, *ACS Appl. Mater. Interfaces*, 2017, **9**, 1145–1153.
189 Z. Chen, Z. Hu, Z. Wu, X. Liu, Y. Jin, M. Xiao, F. Huang and Y. Cao, *J. Mater. Chem. A*, 2017, **5**, 19447–19455.
190 C. Sun, Q. Xue, Z. Hu, Z. Chen, F. Huang, H.-L. Yip and Y. Cao, *Small*, 2015, **11**, 3344–3350.
191 S.-H. Sunwoo, S. I. Han, C. S. Park, J. H. Kim, J. S. Georgiou, S.-P. Lee, D.-H. Kim and T. Hyeon, *Nat. Rev. Bioeng.*, 2024, **2**, 8–24.
192 K.-L. Wang, T.-H. Kuo, C.-F. Yao, S.-W. Chang, Y.-S. Yang, H.-K. Huang, C.-J. Tsai and M. Horie, *Chem. Commun.*, 2017, **53**, 1856–1859.
193 A. Marks, S. Griggs, N. Gasparini and M. Moser, *Adv. Mater. Interfaces*, 2022, **9**, 2102039.
194 J. Rivnay, S. Inal, A. Salleo, R. M. Owens, M. Berggren and G. G. Malliaras, *Nat. Rev. Mater.*, 2018, **3**, 17086.
195 Q. Zhang, T. Jin, X. Ye, D. Geng, W. Chen and W. Hu, *Adv. Funct. Mater.*, 2021, **31**, 2106151.
196 W. Zhong, S. Sun, L. Ying, F. Liu, L. Lan, F. Huang and Y. Cao, *ACS Appl. Mater. Interfaces*, 2017, **9**, 7315–7321.
197 R. B. Rashid, X. Ji and J. Rivnay, *Biosens. Bioelectron.*, 2021, **190**, 113461.
198 D. Khodagholy, J. Rivnay, M. Sessolo, M. Gurfinkel, P. Leleux, L. H. Jimison, E. Stavrinidou, T. Herve, S. Sanaur, R. M. Owens and G. G. Malliaras, *Nat. Commun.*, 2013, **4**, 2133.
199 X. Ji, X. Lin and J. Rivnay, *Nat. Commun.*, 2023, **14**, 1665.
200 S. T. Keene, T. P. A. van der Pol, D. Zakhidov, C. H. L. Weijtens, R. A. J. Janssen, A. Salleo and Y. van de Burgt, *Adv. Mater.*, 2020, **32**, 2000270.
201 F. Hempel, J. K. Y. Law, T. C. Nguyen, R. Lanche, A. Susloparova, X. T. Vu and S. Ingebrandt, *Biosens. Bioelectron.*, 2021, **180**, 113101.
202 K. Tang, W. Miao and S. Guo, *ACS Appl. Polym. Mater.*, 2021, **3**, 1436–1444.
203 J. Hungenberg, A. Hochgesang, F. Meichsner and M. Thelakkat, *Adv. Funct. Mater.*, 2024, **34**, 2407067.
204 S. Inal, J. Rivnay, P. Leleux, M. Ferro, M. Ramuz, J. C. Brendel, M. M. Schmidt, M. Thelakkat and G. G. Malliaras, *Adv. Mater.*, 2014, **26**, 7450–7455.
205 A. T. Lill, D. X. Cao, M. Schrock, J. Vollbrecht, J. Huang, T. Nguyen-Dang, V. V. Brus, B. Yurash, D. Leifert, G. C. Bazan and T.-Q. Nguyen, *Adv. Mater.*, 2020, **32**, 1908120.
206 P. Schmode, D. Ohayon, P. M. Reichstein, A. Savva, S. Inal and M. Thelakkat, *Chem. Mater.*, 2019, **31**, 5286–5295.
207 S. Zhang, P. Kumar, A. S. Nouas, L. Fontaine, H. Tang and F. Cicoira, *APL Mater.*, 2014, **3**, 014911.
208 P. O. Osazuwa, C.-Y. Lo, X. Feng, A. Nolin, C. Dhong and L. V. Kayser, *ACS Appl. Mater. Interfaces*, 2023, **15**, 54711–54720.
209 J. Bai, D. Liu, X. Tian, Y. Wang, B. Cui, Y. Yang, S. Dai, W. Lin, J. Zhu, J. Wang, A. Xu, Z. Gu and S. Zhang, *Sci. Adv.*, 2024, **10**, eadl1856.
210 Y. Li, N. Wang, A. Yang, H. Ling and F. Yan, *Adv. Electron. Mater.*, 2019, **5**, 1900566.
211 X. Xi, D. Wu, W. Ji, S. Zhang, W. Tang, Y. Su, X. Guo and R. Liu, *Adv. Funct. Mater.*, 2020, **30**, 1905361.
212 S. S. L. Andersen, A. D. Jackson and T. Heimburg, *Prog. Neurobiol.*, 2009, **88**, 104–113.
213 T. Li, J. Y. C. Koh, A. Moudgil, H. Cao, X. Wu, S. Chen, K. Hou, A. Surendran, M. Stephen, C. Tang, C. Wang, Q. J. Wang, C. Y. Tay and W. L. Leong, *ACS Nano*, 2022, **16**, 12049–12060.
214 P. Li, J. Shi, Y. Lei, Z. Huang and T. Lei, *Nat. Commun.*, 2022, **13**, 5970.
215 H. Sun, J. Gerasimov, M. Berggren and S. Fabiano, *J. Mater. Chem. C*, 2018, **6**, 11778–11784.
216 H. Liao, J. Chen, L. Lan, Y. Yu, G. Zhu, J. Duan, X. Zhu, H. Dai, M. Xiao, Z. Li, W. Yue and I. McCulloch, *ACS Appl. Mater. Interfaces*, 2022, **14**, 16477–16486.
217 A. F. Paterson, A. Savva, S. Wustoni, L. Tsetseris, B. D. Paulsen, H. Faber, A. H. Emwas, X. Chen, G. Nikiforidis, T. C. Hidalgo, M. Moser, I. P. Maria, J. Rivnay, I. McCulloch, T. D. Anthopoulos and S. Inal, *Nat. Commun.*, 2020, **11**, 3004.
218 Z. S. Parr, J. Borges-González, R. B. Rashid, K. J. Thorley, D. Meli, B. D. Paulsen, J. Strzalka, J. Rivnay and C. B. Nielsen, *Adv. Mater.*, 2022, **34**, 2107829.
219 A. Giovannitti, C. B. Nielsen, D.-T. Sbircea, S. Inal, M. Donahue, M. R. Niazi, D. A. Hanifi, A. Amassian, G. G. Malliaras, J. Rivnay and I. McCulloch, *Nat. Commun.*, 2016, **7**, 13066.

© 2025 The Author(s). Published by the Royal Society of Chemistry

Open Access Article. Published on 14 März 2025. Downloaded on 28.01.2026 01:53:57.
This article is licensed under a Creative Commons Attribution-NonCommercial 3.0 Unported Licence.

220 J. Xie and Y.-C. Lu, *Nat. Commun.*, 2020, **11**, 2499.
221 J. Xiao, F. Shi, T. Glossmann, C. Burnett and Z. Liu, *Nat. Energy*, 2023, **8**, 329–339.
222 T. Kim, W. Song, D.-Y. Son, L. K. Ono and Y. Qi, *J. Mater. Chem. A*, 2019, **7**, 2942–2964.
223 P. K. Nayak, L. Yang, W. Brehm and P. Adelhelm, *Angew. Chem., Int. Ed.*, 2018, **57**, 102–120.
224 Z. Yang, Y. Dai, S. Wang and J. Yu, *J. Mater. Chem. A*, 2016, **4**, 18210–18222.
225 W. Zhao, C. Zhao, H. Wu, L. Li and C. Zhang, *J. Energy Storage*, 2024, **81**, 110409.
226 X. Yue, J. Zhang, Y. Dong, Y. Chen, Z. Shi, X. Xu, X. Li and Z. Liang, *Angew. Chem., Int. Ed.*, 2023, **62**, e202302285.
227 Q. He, J. Ning, H. Chen, Z. Jiang, J. Wang, D. Chen, C. Zhao, Z. Liu, I. F. Perepichka, H. Meng and W. Huang, *Chem. Soc. Rev.*, 2024, **53**, 7091–7157.
228 W. Dou, M. Zheng, W. Zhang, T. Liu, F. Wang, G. Wan, Y. Liu and X. Tao, *Adv. Funct. Mater.*, 2023, **33**, 2305161.
229 P. Das and B. C. Thompson, *Polym. J.*, 2023, **55**, 317–341.
230 S. N. Eliseeva, O. V. Levin, E. G. Tolstopjatova, E. V. Alekseeva, R. V. Apraksin and V. V. Kondratiev, *Mater. Lett.*, 2015, **161**, 117–119.
231 K. Minnici, Y. H. Kwon, L. M. Housel, G. D. Renderos, J. F. Ponder Jr., C. Buckley, J. R. Reynolds, K. J. Takeuchi, E. S. Takeuchi, A. C. Marschilok and E. Reichmanis, *ACS Appl. Energy Mater.*, 2019, **2**, 7584–7593.
232 D. Liu, Y. Zhao, R. Tan, L.-L. Tian, Y. Liu, H. Chen and F. Pan, *Nano Energy*, 2017, **36**, 206–212.
233 X. Chen, C. Zhao, K. Yang, S. Sun, J. Bi, N. Zhu, Q. Cai, J. Wang and W. Yan, *Energy Environ. Mater.*, 2023, **6**, e12483.
234 Y. He, Z. Chang, S. Wu and H. Zhou, *J. Mater. Chem. A*, 2018, **6**, 6155–6182.
235 J. Zhang, Y. Zhou, F. Tu, Y. Ma, H. Zhang, D. Song, X. Shi and L. Zhang, *Chem. Eng. J.*, 2022, **428**, 132510.
236 M. Dent, S. Grabe, O. Ayere, S. Babar, M. G. Masteghin, D. C. Cox, B. J. Howlin, M. A. Baker and C. Lekakou, *ACS Appl. Energy Mater.*, 2024, **7**, 7349–7361.
237 N. Batyrgali, Y. Yerkinbekova, N. Tolganbek, S. Kalybekkyzy, Z. Bakenov and A. Mentbayeva, *ACS Appl. Energy Mater.*, 2023, **6**, 588–604.
238 M. Rana, M. Li, Q. He, B. Luo, L. Wang, I. Gentle and R. Knibbe, *J. Energy Chem.*, 2020, **44**, 51–60.
239 I. Bauer, S. Thieme, J. Brückner, H. Althues and S. Kaskel, *J. Power Sources*, 2014, **251**, 417–422.
240 X. Yu, J. Joseph and A. Manthiram, *J. Mater. Chem. A*, 2015, **3**, 15683–15691.
241 Z. Li, L.-P. Hou, X.-Q. Zhang, B.-Q. Li, J.-Q. Huang, C.-M. Chen, Q.-B. Liu, R. Xiang and Q. Zhang, *Battery Energy*, 2022, **1**, 20220006.
242 A. Wang, G. Xu, B. Ding, Z. Chang, Y. Wang, H. Dou and X. Zhang, *ChemElectroChem*, 2017, **4**, 362–368.
243 R. Yi, X. Lin, Y. Zhao, C. Liu, Y. Li, L. J. Hardwick, L. Yang, C. Zhao, X. Geng and Q. Zhang, *ChemElectroChem*, 2019, **6**, 3648–3656.
244 C. L. Anderson, N. Dai, S. J. Teat, B. He, S. Wang and Y. Liu, *Angew. Chem., Int. Ed.*, 2019, **58**, 17978–17985.
245 X. Ye, J. Zhang, H. Chen, X. Wang and F. Huang, *ACS Appl. Mater. Interfaces*, 2014, **6**, 5113–5121.
246 P. Chen, Y. Ma, Z. Zheng, C. Wu, Y. Wang and G. Liang, *Nat. Commun.*, 2019, **10**, 1192.
247 X. Lin, Y. Liang, Z. Hu, X. Zhang, Y. Liang, Z. Hu, F. Huang and Y. Cao, *Nanomaterials*, 2022, **12**, 1535.
248 H. Nishiyama, T. Yamada, M. Nakabayashi, Y. Maehara, M. Yamaguchi, Y. Kuromiya, Y. Nagatsuma, H. Tokudome, S. Akiyama, T. Watanabe, R. Narushima, S. Okunaka, N. Shibata, T. Takata, T. Hisatomi and K. Domen, *Nature*, 2021, **598**, 304–307.
249 Y. Wang, A. Vogel, M. Sachs, R. S. Sprick, L. Wilbraham, S. J. A. Moniz, R. Godin, M. A. Zwijnenburg, J. R. Durrant, A. I. Cooper and J. Tang, *Nat. Energy*, 2019, **4**, 746–760.
250 Y. Wu, X. Zhang, Y. Xing, Z. Hu, H. Tang, W. Luo, F. Huang and Y. Cao, *ACS Mater. Lett.*, 2019, **1**, 620–627.
251 Y. Liu, B. Li and Z. Xiang, *Small*, 2021, **17**, 2007576.
252 F. Lodola, V. Rosti, G. Tullii, A. Desii, L. Tapella, P. Catarsi, D. Lim, F. Moccia and M. R. Antognazza, *Sci. Adv.*, 2019, **5**, eaav4620.
253 Y. Yuan, Y. Min, Q. Hu, B. Xing and B. Liu, *Nanoscale*, 2014, **6**, 11259–11272.
254 M. Overchuk, R. A. Weersink, B. C. Wilson and G. Zheng, *ACS Nano*, 2023, **17**, 7979–8003.
255 L. Hu, Z. Chen, X. Su, Y. Liu, T. Guo, R. Liu, B. Tian, C. Wang and L. Ying, *J. Mater. Chem. B*, 2020, **8**, 10609–10615.
256 B. E. Logan, R. Rossi, A. A. Ragab and P. E. Saikaly, *Nat. Rev. Microbiol.*, 2019, **17**, 307–319.
257 Z. Chen, G. Quek, J.-Y. Zhu, S. J. W. Chan, S. J. Cox-Vázquez, F. Lopez-Garcia and G. C. Bazan, *Angew. Chem., Int. Ed.*, 2023, **62**, e202307101.
258 A. A. Mier, H. Olvera-Vargas, M. Mejía-López, A. Longoria, L. Verea, P. J. Sebastian and D. M. Arias, *Chemosphere*, 2021, **283**, 131138.
259 F. Harnisch and U. Schröder, *Chem. Soc. Rev.*, 2010, **39**, 4433–4448.
260 G. Quek, S. R. McCuskey, R. J. Vázquez, S. J. Cox-Vázquez and G. C. Bazan, *Adv. Electron. Mater.*, 2023, **9**, 2300019.
261 G. Quek, R. J. Vázquez, S. R. McCuskey, B. Kundukad and G. C. Bazan, *Adv. Mater.*, 2022, **34**, 2203480.
262 Y. Meng, J. Gao, X. Huang, P. Liu, C. Zhang, P. Zhou, Y. Bai, J. Guo, C. Zhou, K. Li, F. Huang and Y. Cao, *Adv. Mater.*, 2025, 2415705, DOI: **10.1002/adma.202415705**.
263 C. Zhou, S. J. Cox-Vázquez, G. W. N. Chia, R. J. Vázquez, H. Y. Lai, S. J. W. Chan, J. Limwongyut and G. C. Bazan, *Sci. Adv.*, 2023, **9**, eade2996.
264 C. Zhou, Z. Li, Z. Zhu, G. W. N. Chia, A. Mikhailovsky, R. J. Vázquez, S. J. W. Chan, K. Li, B. Liu and G. C. Bazan, *Adv. Mater.*, 2022, **34**, 2201989.
265 Y. Meng, J. Gao, P. Zhou, X. Qin, M. Tian, X. Wang, C. Zhou, K. Li, F. Huang and Y. Cao, *Angew. Chem., Int. Ed.*, 2024, **63**, e202318632.
266 Q. Kang, L. Ye, B. Xu, C. An, S. J. Stuard, S. Zhang, H. Yao, H. Ade and J. Hou, *Joule*, 2019, **3**(1), 227–239.

© 2025 The Author(s). Published by the Royal Society of Chemistry